2023-10-09

Calculation of ATP production rates using the Seahorse XF Analyzer

Desousa, BR

10.15252/embr.202256380
EMBO reports
EMBO

Article

SOURCE DATA | TRANSPARENT PROCESS | OPEN ACCESS

EMBO reports

Calculation of ATP production rates using the Seahorse XF Analyzer

Brandon R Desousa[1], Kristen KO Kim[1], Anthony E Jones[1], Andréa B Ball[1], Wei Y Hsieh[2], Pamela Swain[3], Danielle H Morrow[1], Alexandra J Brownstein[4], David A Ferrick[3], Orian S Shirihai[4], Andrew Neilson[3], David A Nathanson[1], George W Rogers[3], Brian P Dranka[3], Anne N Murphy[5], Charles Affourtit[6], Steven J Bensinger[2], Linsey Stiles[1,4], Natalia Romero[3] & Ajit S Divakaruni[1,*]

Abstract

Oxidative phosphorylation and glycolysis are the dominant ATP-generating pathways in mammalian metabolism. The balance between these two pathways is often shifted to execute cell-specific functions in response to stimuli that promote activation, proliferation, or differentiation. However, measurement of these metabolic switches has remained mostly qualitative, making it difficult to discriminate between healthy, physiological changes in energy transduction or compensatory responses due to metabolic dysfunction. We therefore present a broadly applicable method to calculate ATP production rates from oxidative phosphorylation and glycolysis using Seahorse XF Analyzer data and empirical conversion factors. We quantify the bioenergetic changes observed during macrophage polarization as well as cancer cell adaptation to *in vitro* culture conditions. Additionally, we detect substantive changes in ATP utilization upon neuronal depolarization and T cell receptor activation that are not evident from steady-state ATP measurements. This method generates a single readout that allows the direct comparison of ATP produced from oxidative phosphorylation and glycolysis in live cells. Additionally, the manuscript provides a framework for tailoring the calculations to specific cell systems or experimental conditions.

Keywords ATP; ECAR; glycolysis; oxidative phosphorylation; Seahorse XF Analyzer

Subject Categories Immunology; Metabolism; Methods & Resources

DOI 10.15252/embr.202256380 | Received 26 October 2022 | Revised 5 July 2023 | Accepted 14 July 2023

EMBO Reports (2023) e56380

Introduction

ATP is critical for cellular energy transduction. Essential cellular functions such as maintenance of ion homeostasis, macromolecule biosynthesis, motility, and autophagy involve reactions coupled to ATP hydrolysis to support these otherwise energetically unfavorable processes. The two dominant ATP-producing pathways in mammalian cells are glycolysis and oxidative phosphorylation (Chandel, 2015). Glycolysis involves the cytoplasmic breakdown of one molecule glucose into two molecules of pyruvate, generating two molecules of ATP in the process. The fermentation of pyruvate to lactate and subsequent lactate efflux enables continuous glycolytic turnover. Pyruvate and other carbon-rich energy substrates such as fatty acids and amino acids can also be taken up by mitochondria and completely oxidized during oxidative phosphorylation. The chemical energy in these substrates is converted to potential energy by the mitochondrial respiratory chain, and this reservoir of potential energy is used to drive ATP synthesis (Rich & Maréchal, 2010; Nicholls & Ferguson, 2013).

It is now clear that redistributing the balance between oxidative phosphorylation and glycolysis can characterize – and in some cases determine – cell function and fate (Lunt & Vander Heiden, 2011; Sullivan *et al*, 2018; DeBerardinis & Chandel, 2020; Shin *et al*, 2020). Glycolysis and offshoot pathways play essential roles in generating precursors for macromolecule biosynthesis (Lunt & Vander Heiden, 2011), supporting one-carbon metabolism (Ducker & Rabinowitz, 2017), and establishing cytoplasmic reducing power (Lewis *et al*, 2014). Biological processes such as stem cell pluripotency (Gu *et al*, 2016), oncogenesis (DeBerardinis & Chandel, 2020), growth factor signaling (Pavlova & Thompson, 2016), and immune cell activation (van den Bossche *et al*, 2017) are therefore frequently associated with a preferential shift towards glycolysis. Conversely, terminal differentiation is often accompanied by an increased capacity for oxidative phosphorylation and the complete oxidation of

1 Department of Molecular and Medical Pharmacology, University of California, Los Angeles, Los Angeles, CA, USA
2 Department of Microbiology, Immunology, and Molecular Genetics, University of California, Los Angeles, Los Angeles, CA, USA
3 Agilent Technologies, Santa Clara, CA, USA
4 Department of Medicine, University of California, Los Angeles, Los Angeles, CA, USA
5 Cytokinetics Inc., South San Francisco, CA, USA
6 School of Biomedical Sciences, University of Plymouth, Plymouth, UK
*Corresponding author. Tel: +1 (310) 825 8630; E-mail: adivakaruni@mednet.ucla.edu

glucose and fatty acids (Moyes *et al*, 1997; Wilson-Fritch *et al*, 2003; Chen *et al*, 2008; Divakaruni *et al*, 2014; Hazim *et al*, 2022).

Despite the importance of cellular ATP production rates and the distribution between glycolysis and oxidative phosphorylation, common measurement approaches are often limiting. Snapshot measurements of cellular ATP content are routinely used to characterize changes in energy metabolism, but these are generally informative only in extreme cases of energetic dysfunction such as ischemia (Brand & Nicholls, 2011). During physiological cell activation, cells can readily increase the rate of ATP production to match the increased rate of consumption without appreciably changing steady-state ATP levels. A far more useful metric is the ATP:ADP ratio, reflecting the free energy change associated with ATP hydrolysis into ADP and inorganic phosphate. However, biochemical or mass spectrometry-based approaches to measure ATP:ADP are limiting. They are destructive measurements conducted on cell lysates, and therefore unable to measure real-time changes. They are also prone to experimental noise that masks subtle but meaningful differences. Kinetic measurements of energy status are therefore extraordinarily specialized, requiring transfection of a genetically engineered ATP:ADP sensor and an expert understanding of the caveats involved when using molecular probes (Tantama & Yellen, 2014; Koveal *et al*, 2020). Importantly, all these approaches lack direct information about whether the measured ATP is derived from oxidative phosphorylation or glycolysis.

Fluorescence-based, multi-well technologies such as Seahorse XF Analysis can characterize these bioenergetic shifts, as simultaneous measurements of oxygen consumption rates (OCR) and extracellular acidification rates (ECAR) can gauge the relative balance between oxidative phosphorylation and glycolysis (Pelletier *et al*, 2014; Divakaruni & Jastroch, 2022; i.e. OCR:ECAR ratio). However, precise quantification of the total rate of ATP production and the balance between these two pathways is not straightforward. Direct comparison is precluded by differences in unit scale between OCR (pmol O_2/min) and ECAR (mpH/min). Quantitative comparison between the two pathways is further confounded by the differential ATP yields from each pathway: for oxidation of one molecule of glucose, the maximum glycolytic yield is 2 ATP as opposed to 33.45 ATP for oxidative phosphorylation (Mookerjee *et al*, 2017). As such, a large increase in acidification of the extracellular medium may not necessarily indicate a rebalancing of ATP production if it is matched with even a marginal increase in oxygen consumption.

Additionally, ECAR measurements can be influenced by cellular processes other than lactate efflux that also result in a net acidification of the extracellular medium. Indeed, the main component of ECAR in two-dimensional cell culture systems is often glycolysis and fermentation (McConnell *et al*, 1992), reflecting the uptake of uncharged glucose and the release of anionic lactate. However, other acidifying reactions can contribute to the measured ECAR. For example, CO_2 evolution during oxidative metabolism (e.g. dehydrogenases of the TCA cycle or the pentose phosphate pathway) acidifies the medium after hydration and generation of bicarbonate ($CO_2 + H_2O \rightarrow H_2CO_3 \rightarrow H^+ + HCO^{3-}$). Additionally, specific cell types can release appreciable amounts of organic acids such as pyruvate (Hong *et al*, 2016), glutamate (Divakaruni *et al*, 2017), or fatty acids (Thompson *et al*, 2010) that may be reflected in ECAR measurements. As such, the extracellular acidification rate cannot itself quantify lactate efflux (Newell *et al*, 1993; Gillies *et al*, 2008; Divakaruni *et al*, 2014).

We therefore applied a method to transform OCR and ECAR into rates of ATP production from oxidative phosphorylation and glycolysis. Although measurements of OCR and ECAR have become a central cell biology technique, the qualitative nature of the analysis makes it difficult to discriminate between healthy, physiological shifts in bioenergetic pathways or compensatory responses due to mitochondrial dysfunction. This method detailed here provides a solution to this challenge in a single, live cell readout estimating the total rate of cellular ATP production as well as its distribution between oxidative phosphorylation and glycolysis. The theoretical foundation and approach to convert OCR and ECAR to rates of oxidative phosphorylation and glycolysis have been published, though the conversion factors obtained from the largely empirical strategy presented here differ substantively from previous work (Mookerjee *et al*, 2015; Mookerjee *et al*, 2017). Model parameters are formed with data from over 20 primary and immortalized cell lines, and the analysis detects substantive changes not evident from steady-state ATP measurements.

Results

Validation of the method

The Seahorse XF Analyzer provides kinetic readouts of the oxygen consumption rate (OCR; in pmol O_2/min) and extracellular acidification rate (ECAR; in mpH/min). These measurements very often correlate with oxidative phosphorylation (OCR) and glycolysis (ECAR), but do not directly reflect the quantity of ATP produced via each pathway (Divakaruni *et al*, 2014). A strategy to convert OCR and ECAR readings into rates of ATP produced from oxidative phosphorylation and glycolysis involved three principal steps (Mookerjee *et al*, 2015; Mookerjee *et al*, 2017):

i Transforming ECAR (mpH/min) into a proton production rate (pmol H^+/min) so rates of medium acidification could be directly compared against rates of oxygen consumption (pmol O_2/min) or lactate efflux (pmol lactate/min) with similar units.
   a. mpH/min → pmol H^+/min
ii Accounting for sources of acidification not associated with glycolysis and fermentation so changes in H^+ production quantitatively reflect lactate efflux.
   a. pmol H^+/min → pmol $H^+_{lactate}$/min
iii Converting rates of oxygen consumption and lactate efflux into ATP produced from oxidative phosphorylation and glycolysis using established stoichiometry.
   a. pmol O_2/min → pmol ATP_{OxPhos}/min
   b. pmol $H^+_{lactate}$/min → pmol ATP_{Glyco}/min
   c. pmol ATP/min = pmol ATP_{OxPhos}/min + pmol ATP_{Glyco}/min

The work presented uses a 96-well Seahorse XF Analyzer platform. Although some values cannot be directly translated to 24-well instruments due to differences in volume of the measurement microchamber, the experimental strategy to calculate these values is universal across all Seahorse XF platforms.

Transforming ECAR into a proton production rate

It was first necessary to convert ECAR into values of pmol H^+/min so rates of medium acidification could be easily compared against

OCR (in pmol O_2/min) and parallel lactate efflux assays (in pmol lactate/min). This unit conversion required calculating the buffering power of the experimental medium. Buffering power is defined here as the pH change in the measurement microchamber elicited by a given amount of H^+ (Fig 1A). Importantly, sequential additional of H_2SO_4 showed the change in pH was directly proportional to the added H^+ over a range greater than 0.5 pH units (Fig 1B). Predictably, as the concentration of HEPES in the medium increased, there

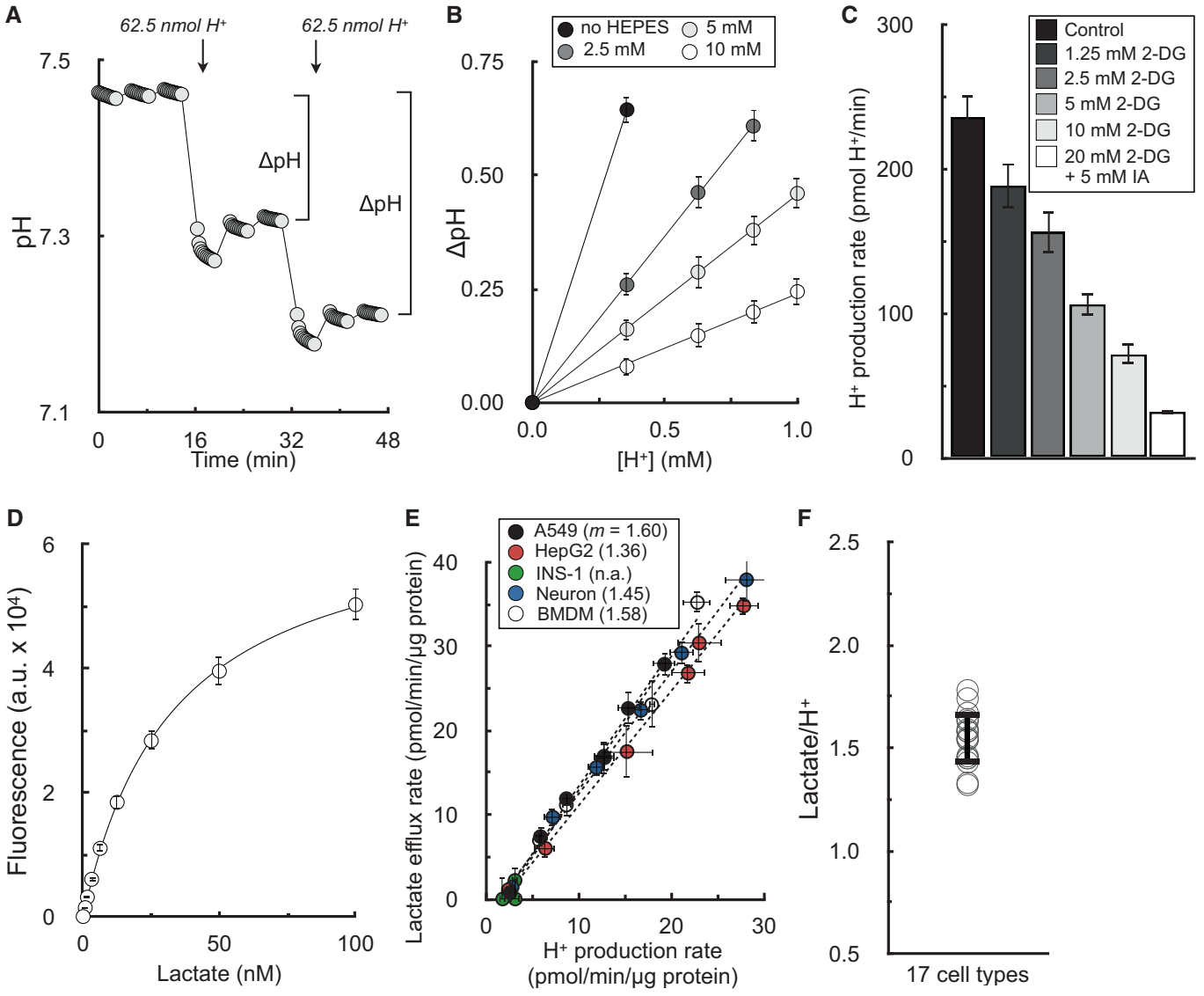

Figure 1. Extracellular acidification is directly proportional to lactate efflux in the absence of respiration.

A Sample trace of H_2SO_4 injections to determine buffer capacity of Seahorse experimental medium. Error bars are obscured by the symbol (n = 16 technical replicates from a single experiment).

B Changes in pH from sequential additions of 62.5 nmol H^+ via the injector ports. The experimental medium is DMEM supplemented with 8 mM glucose, 2 mM glutamine, 2 mM pyruvate, and the indicated concentration of HEPES (pH 7.4). The microchamber volume of the 96-well XF Analyzer is 2.28 µl. Step-by-step calculations are available in Dataset EV1 (n = 6 experimental replicates).

C The H^+ production rate is given for A549 cells treated acutely (20 min prior to assay) with varying concentrations of 2-deoxyglucose (2DG) or 2DG with iodoacetic acid (IAA) to block glycogenolysis. The experimental medium contains 5 mM glucose with 5 mM HEPES, 200 nM rotenone (complex I inhibitor), 1 µM antimycin (complex III inhibitor), and 2 µM oligomycin (complex V inhibitor to block 'reverse' hydrolysis of ATP upon respiratory chain inhibition) (n = 6 biological replicates).

D Sample trace of standard curve used to measure lactate collected from experimental medium (n = 3 technical replicates).

E Plot of lactate efflux rates measured as in (D) against H^+ production rates measured in the Seahorse XF Analyzer. Experimental conditions and titration of the rate with glycolytic inhibitors are as in (C). Parenthetical values given in the key are the fitted slopes for each individual cell type (n = 6 biological replicates).

F Aggregate lactate:H^+ ratios, calculated as in (E) for 17 different cell types, yielding an average value of 1.53 ± 0.12 (mean ± standard deviation).

All data are mean ± S.E.M. unless otherwise specified.
Source data are available online for this figure.

was a smaller drop in pH elicited from the added H^+. The results demonstrate that extracellular acidification measurements in mpH/min are readily converted to values of pmol H^+/min by applying a scalar factor accounting for the buffering power of the medium and the volume of the measurement microchamber. Sample calculations and step-by-step instructions for transforming ECAR into values of pmol H^+/min are provided in the Datasets EV1 and EV2.

Accounting for sources of acidification other than lactate efflux

It was then necessary to determine whether measurements of H^+ efflux could indeed accurately measure lactate efflux. In principle, there could be several reactions that could cause a meaningful net pH change in the experimental medium in addition to the incomplete oxidation of uncharged glucose into anionic lactate (Fig EV1A). Other glycolysis-linked reactions can result in medium acidification, such as the efflux of anionic pyruvate or CO_2 evolution during the oxidative pentose phosphate pathway (Fig EV1B). Additionally, several mitochondrial dehydrogenases will generate CO_2 during the complete oxidation of energy substrates and oxidative phosphorylation. These include the 2-oxoacid dehydrogenase family (pyruvate dehydrogenase, α-ketoglutarate dehydrogenase, and the branched chain keto acid dehydrogenase) and isocitrate dehydrogenase (Fig EV1C). Furthermore, specific cell types may release organic acids under certain conditions, such as hepatocyte efflux of ketone bodies during robust fatty acid oxidation or neuronal release of glutamate during prolonged depolarization.

Rather than attempt to account for every possible acidifying reaction, we began by testing the hypothesis that respiratory acidification (CO_2 evolution from mitochondrial dehydrogenases linked to O_2 consumption) would be the only acidifying process with a large enough flux to affect the measurements on a scale comparable with lactate efflux in the basal state. If this hypothesis is correct, then the following testable predictions should hold. First, if respiratory acidification is indeed the only measurable source of non-glycolytic acidification, any remaining acid production should be attributable to glycolysis when respiration is inhibited. Similarly, in the absence of glycolysis, respiration should be directly proportional to the remaining acidification rate.

In the absence of respiration, glycolysis is the exclusive source of measurable extracellular acidification

We first measured whether lactate efflux was directly proportional to H^+ production after chemical inhibition of the respiratory chain. In the presence of electron transport chain inhibitors, cellular H^+ production was gradually reduced with increasing concentrations of glycolytic inhibitors in A549 cells (Fig 1C). We then measured the lactate content in the spent experimental medium from these samples using an enzymatic lactate assay (Fig 1D) to determine the relationship between lactate efflux and acid production in the absence of respiration (Fig 1E). As a negative control, no measurable acidification was observed in cultured pancreatic β-cells (Zhao *et al*, 2001), which do not express appreciable levels of lactate dehydrogenase or monocarboxylate transporter-1. Using 17 different cell types comprised of primary and immortalized cultures, this analysis yielded an average lactate:H^+ ratio of 1.53 ± 0.12 (Fig 1F; Appendix Table S1).

Unexpectedly, this value deviated from our expectations and was substantially different from previous efforts to correlate H^+ production and lactate efflux rates (Mookerjee *et al*, 2015). In principle, the lactate:H^+ ratio should never be greater than 1, since lactate efflux should never exceed the total H^+ efflux given their 1:1 stoichiometry. In fact, the theoretical lactate:H^+ should be < 1 due to acidifying reactions associated with glycolysis but distinct from lactate efflux (Fig EV1B). We reasoned that this discrepancy could be due to the incomplete coverage of the measurement well by the fluorometric sensor of the Seahorse XF cartridge: although the enzymatic lactate measurements used medium collected from the entire well, outer portions of the well are likely undetected by the fluorometric sensor spot(s) during the acidification measurements (Gerencser *et al*, 2009; Fig EV2A).

To test this, we scraped cells from the measurement well from either the center of the three risers directly under the sensor (creating a "donut" shape of cells in the well) or on the rim of the plate outside the three risers (leaving cells in the center untouched; Fig EV2B). As predicted, both OCR and ECAR were significantly reduced when cells in the middle of the well were removed, but losing cells along the outer rim did not significantly affect the measurements (Fig EV2C). To ensure the results were not due to changes in cell number, the lactate:H^+ ratio was calculated for these conditions. Consistent with the sensor not seeing the outer edges of the well, lactate:H^+ was lowered close to 1 when cells were removed from the outer rim, and increased beyond 8 when cells were removed from center of the plate (Fig EV2D). Rather than a systemic error with the buffer capacity or enzymatic measurements, the result demonstrates that incomplete sensor coverage of the measurement well is a main driver of why lactate:H^+ values deviate from theoretical expectations.

In the absence of glycolysis, respiration is the exclusive source of measurable medium acidification

Having shown that medium acidification is tightly correlated with glycolysis in the absence of respiration in Fig 1, we then tested whether medium acidification would be tightly correlated to respiration in the absence of glycolysis. We therefore measured acidification rates in HepG2 cells offered glucose-free medium containing pyruvate, glutamine, and the glycolytic inhibitors 2-deoxyglucose and iodoacetate. The rates of respiration and acidification were titrated by adjusting flux through the electron transport chain (with oligomycin, FCCP, and rotenone with antimycin A) and blocking substrate uptake and oxidation (with varying concentrations of the mitochondrial pyruvate carrier inhibitor UK5099 and the glutaminase inhibitor BPTES; Fig 2A and B).

We observed a proportional relationship between respiration and medium acidification in the absence of glycolysis (Fig 2C). Furthermore, we again extended this analysis to a panel of 21 different primary and immortalized cell preparations to yield an average H^+:O_2 ratio of 0.38 ± 0.05 (Fig 2D; Appendix Table S2). However, similarly to the values obtained for lactate:H^+, the composite H^+:O_2 again deviated sharply from expectations and previous attempts to correct ECAR for respiratory acidification. The value obtained was much lower than the theoretical H^+:O_2 of complete oxidation of either pyruvate (0.80) or glutamine (0.67; Mookerjee *et al*, 2015).

As such, we conducted a series of experiments to better understand the factors that shape the H^+:O_2 value and whether experimental perturbations would change respiratory acidification in expected ways. We first examined whether oxidation of different substrates would perturb H^+:O_2 values, as complete oxidation of

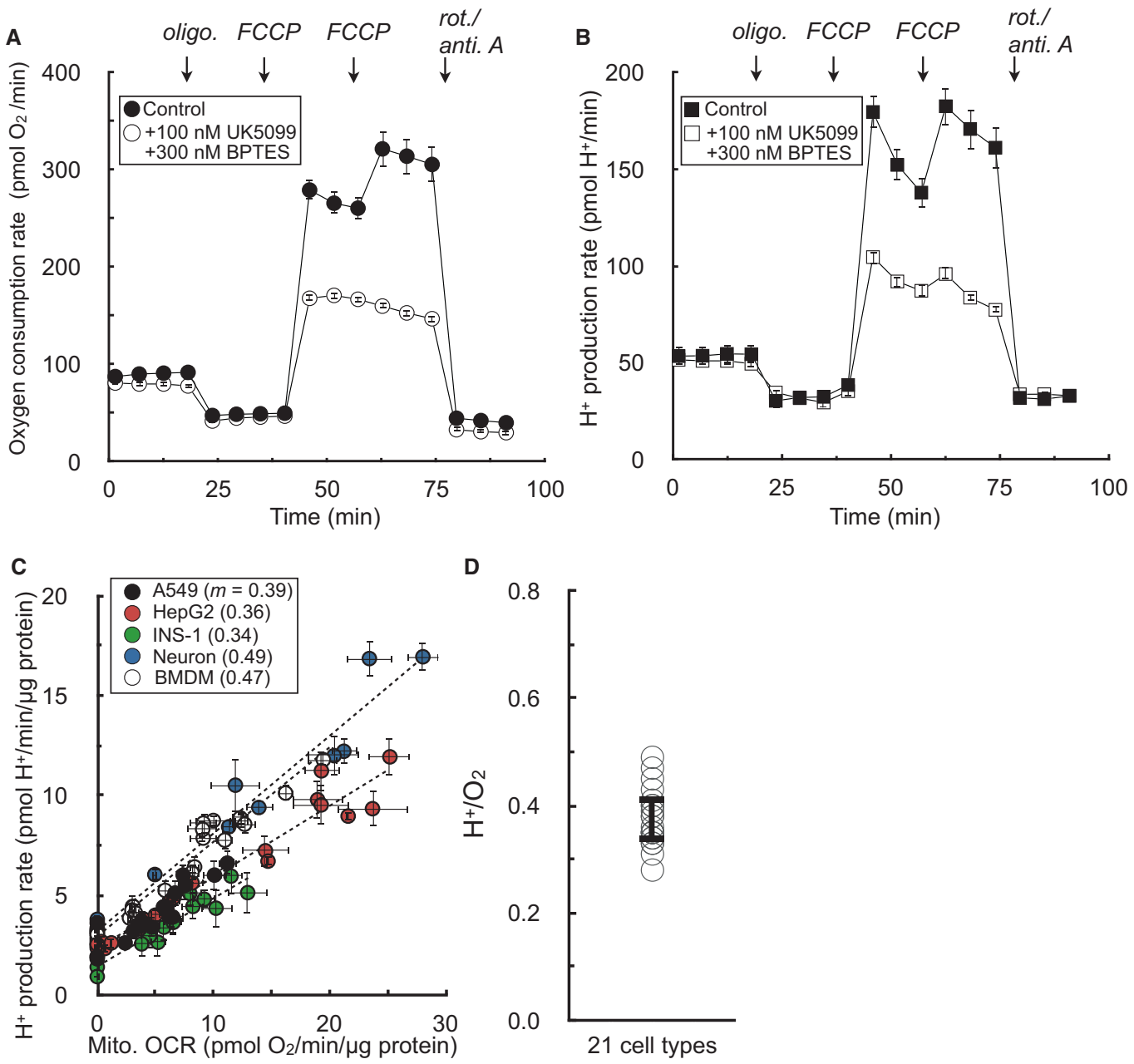

Figure 2. Extracellular acidification is directly proportional to respiration in the absence of glycolysis.

A Sample kinetic trace of oxygen consumption in HepG2 cells in medium containing 5 mM pyruvate, 5 mM glutamine, 5 mM HEPES, 2 mM 2-deoxyglucose, and 50 µM iodoacetate. Where indicated, the respiratory rate was modulated with addition of UK5099 (MPC inhibitor to block pyruvate oxidation) and BPTES (glutaminase inhibitor to block glutamine oxidation) (n = 8 technical replicates from a single experiment).

B Sample kinetic trace of H^+ production rates measured from (A) (n = 8 technical replicates from a single experiment).

C Plot of H^+ production rates against oxygen consumption rates for experiments conducted as in (A & B). The rates are titrated with mitochondrial effectors (oligomycin, varying concentrations of FCCP, rotenone/antimycin A) or combined treatment with UK5099 and BPTES. Individual points are taken as the average values for all measurements for a particular treatment (e.g. average of three measurements in response to initial FCCP addition). Parenthetical values given in the key are the fitted slopes for each individual cell type (n = 6 biological replicates).

D Aggregate H^+:O_2 ratios, calculated as in (C) for 21 different cell types, yielding an average value of 0.38 ± 0.05 (mean ± standard deviation).

All data are mean ± S.E.M. unless otherwise specified.
Source data are available online for this figure.

various substrates yields varying H^+:O_2 ratios. Indeed, the H^+:O_2 ratio resulting from pure glutamine oxidation was fractionally lower than pure pyruvate oxidation (Fig EV3A–C).

We then further examined whether choice of respiratory substrates could influence H^+:O_2 ratios in isolated mitochondria, a simplified system where the experimental conditions are highly

controlled and metabolic reactions can be well defined. We tested acidification from uncoupled respiration in rat heart mitochondria offered (i) pyruvate with malate (P/M), (ii) P/M and inhibitors of multiple enzymes creating a truncated TCA cycle (P/M truncated; Mookerjee *et al*, 2015), and (iii) succinate with rotenone (S/R). The results qualitatively exhibited the expected behavior: the H^+/O_2 ratio for mitochondria oxidizing P/M increased in the presence of inhibitors which blocked downstream TCA cycle reactions (e.g. the alkalinizing succinyl CoA synthetase reaction). Moreover, succinate oxidation in the presence of rotenone, which will support oxygen consumption without generating CO_2, shows robust respiratory rates with negligible changes in pH (Fig EV3D and E).

However, even in this reductionist system, the measured H^+:O_2 fell far below expected values (theoretical H^+:O_2 of P/M truncated = 1). We therefore used the XF24 system to further ensure that the result was not a peculiarity of an individual instrument platform. Using the same workflow as before, and accounting for the larger microchamber volume of the 24-well platform, nearly identical results were observed where respiratory acidification in isolated mitochondria fell short of theoretical predictions (Fig EV3F).

Lastly, in addition to showing that respiratory substrates could affect the H^+:O_2 ratio, we wanted to determine whether forced efflux of organic acids other than lactate could also affect the measurements in predictable ways. For a proof-of-concept example, we measured whether NMDA-induced efflux of glutamate would alter the H^+:O_2 in primary cortical neurons. Neurons were offered exclusively β-hydroxybutyrate with glycolytic inhibitors, so lactate efflux or sources of glycolytic acid production could not interfere with the measurements. As expected, NMDA-induced efflux of glutamate in primary cortical neurons caused a pronounced spike in the acidification rate (Fig EV3G) and the H^+:O_2 ratio (Fig EV3H) that was sensitive to the NMDA-receptor antagonist MK801 (Divakaruni *et al*, 2017). The result was not attributable to glycolysis, as lactate efflux was negligible and unchanged across conditions (Fig EV3I). Taken together, the demonstration that H^+/O_2 ratios respond in expected ways to changes in substrate oxidation and non-glycolytic acid efflux provided additional confidence in the accuracy of the measured values.

Converting rates of oxygen consumption and lactate efflux into ATP produced from oxidative phosphorylation and glycolysis

The results from Figs 1 and 2 demonstrate that rates of H^+ production can, in principle, quantify lactate efflux after correcting for respiratory acidification and accounting for the sensor coverage of the plate well. We therefore transformed H^+ production rates into lactate efflux rates in equation (1) as follows:

$$\text{pmol lactate/min} = 1.53^* \left(H^+_{\text{Total}} - 0.38^* \text{OCR}_{\text{Mito.}}\right), \quad (1)$$

where 1.53 = average lactate:H^+ value obtained in Fig 1; H^+_{Total} = H^+ production rates read by the instrument; 0.38 = average H^+:O_2 value obtained in Fig 2; $\text{OCR}_{\text{Mito.}}$ = basal mitochondrial respiration.

To validate whether these average values obtained under constrained conditions could be broadly applied across different cell types under typical assay conditions (i.e. complete assay medium with both glycolysis and oxidation phosphorylation functional), we compared lactate efflux calculated using the XF Analyzer against an enzymatic assay in A549 adenocarcinoma cells, C2C12 myoblasts, and murine BMDMs (Fig 3A). Prior to adjusting the measurements as in equation (1), the H^+ production rate underestimated the rate of lactate efflux (comparing leftmost bars in each graph with rightmost). But as expected, Seahorse XF measurements accounting for respiratory acidification and sensor coverage resulted in lactate efflux values (middle bars) that matched enzymatic measurements. Taken together with Fig 1, the results suggest the consensus values and approximations used here should be applicable across a broad range of cell types under normal assay conditions.

The ability to quantify lactate efflux with rates of H^+ production allows the transformation of ECAR into a rate of ATP produced by glycolysis. All necessary parameters are obtained during standard respirometry profiling (Fig 3B and C), and sample calculations with representative data sets are available in Datasets EV2–EV4.

The rate of mitochondrial ATP production can be estimated by applying a P:O ratio (moles of ADP phosphorylated per mole of oxygen consumed) to the respiration that drives ATP synthesis (Brand, 2005), which is determined using sensitivity to the ATP synthase inhibitor oligomycin. As detailed elsewhere, oligomycin-sensitive respiration will slightly underestimate ATP-linked respiration (due to overestimating proton leak), though this is a small, ~10% overestimate which can be adjusted ($0.1^*\text{OCR}_{\text{Leak}}$ in equation 2; Affourtit & Brand, 2009). Moreover, assumptions must be made for the selection of P/O ratio based on which substrate is being oxidized. Here, we use a value of P:O = 2.73 (P:O_2 = 5.45), the maximum value for complex I-driven respiration (Watt *et al*, 2010) and within the range of values for complete glucose oxidation (Mookerjee *et al*, 2017). The rate of ATP from oxidative phosphorylation can therefore be estimated as in equation (2):

$$\text{ATP}_{\text{OxPhos}} = 5.45^*\left(\text{OCR}_{\text{ATP}} + 0.1^*\text{OCR}_{\text{Leak}}\right) \quad (2)$$

where 5.45 = P:O_2 (moles of ADP phosphorylated per O_2 consumed); OCR_{ATP} = ATP-linked respiration (respiration sensitive to oligomycin); OCR_{Leak} = Respiration associated with proton leak (respiration insensitive to oligomycin).

The rate of glycolytic ATP production can be estimated with 1:1 stoichiometry to the lactate efflux rate (equation 1), and the total ATP production rate is given by the sum of equations (1) and (2). See Datasets EV2–EV4 for sample calculations.

$$\text{ATP}_{\text{Glyco.}} = \text{Equation 1.} \quad (3)$$

$$\text{ATP}_{\text{Total}} = \text{ATP}_{\text{OxPhos.}} + \text{ATP}_{\text{Glyco.}} \quad (4)$$

Notably, this calculation will slightly underestimate rates of glycolytic ATP, as it fails to account for the ATP generated during glycolysis when glucose-derived pyruvate is funneled into mitochondria for complete oxidation (Mookerjee *et al*, 2017). Accounting for this would require knowing (or assuming) the fractional contribution of glucose oxidation to oxidative phosphorylation relative to other substrates. To test whether this omission would appreciably affect experimental conclusions, we measured rates of ATP production in A549 cells offered complete medium or a simple salts medium supplemented with only glucose. Offering cells only glucose in simple salts allowed calculation of this additional glycolytic ATP by applying known stoichiometry and assuming respiration is exclusively driven by glucose oxidation with no

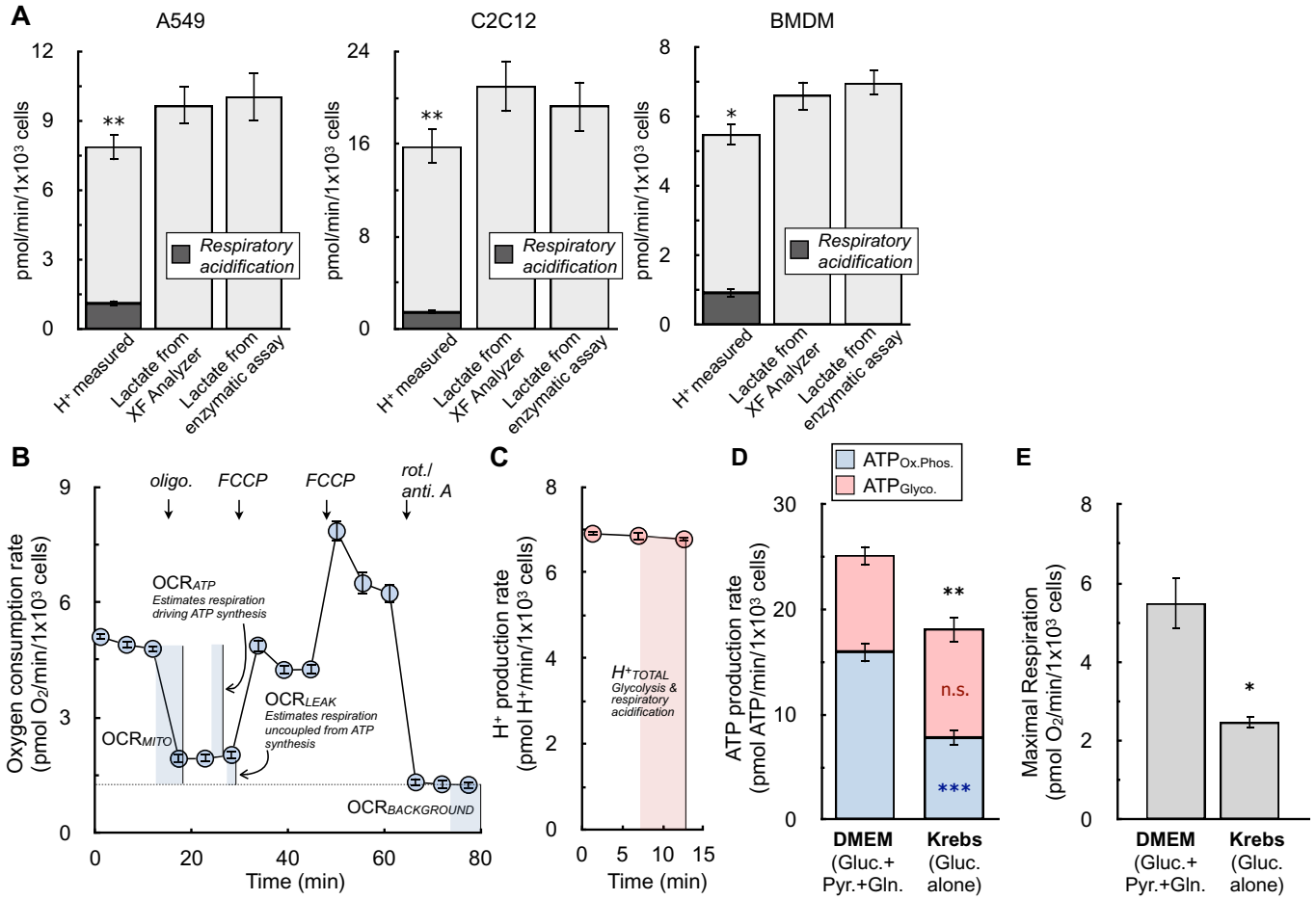

Figure 3. Transformation of ECAR into lactate efflux allows calculation of ATP production rates.

A The H^+ production rate from the XF Analyzer (left bar in each graph), the calculated lactate efflux rate from the XF Analyzer (center bar), and the lactate efflux rate measured from an enzymatic assay (right bar) are given for A549 cells, C2C12 cells, and primary bone marrow-derived macrophages (BMDMs). Cells are offered 8 mM glucose, 2 mM pyruvate, and 2 mM glutamine in experimental medium supplemented with 5 mM HEPES. The shaded component of the H^+ production rates for each cell type is the calculated contribution from respiratory acidification ($n \geq 4$ biological replicates).

B The oxygen consumption rate from a representative experiment with A549 cells is presented. Assay medium is as in (A). The parameters needed to calculate the ATP production rate are indicated within the figure ($n = 6$ technical replicates).

C The H^+ production rate from the kinetic trace in (B) is presented. Only the initial rates are shown, as these are the only measurements required to calculate the ATP production rate ($n = 6$ technical replicates).

D ATP production rates calculated for A549 cells in DMEM supplemented with 8 mM glucose, 2 mM glutamine, and 2 mM pyruvate and Krebs–Henseleit buffer supplemented with only 10 mM glucose ($n = 4$ biological replicates).

E Maximal respiratory rates measured in response to oligomycin and FCCP for treatments as in (D) ($n = 4$ biological replicates).

All data are mean ± S.E.M. Statistical analysis for 3A was analyzed by a one-way, repeated measures ANOVA followed by Dunnett's *post hoc* multiple comparisons tests. Individual pairwise comparisons for 3D and 3E were analyzed by a two-tailed Student's *t*-test. $^*P < 0.05$; $^{**}P < 0.01$; $^{***}P < 0.001$.
Source data are available online for this figure.

contribution from endogenous substrate stores. However, rates of both oxidative phosphorylation and uncoupler-stimulated respiration were substantially limited when cells were offered medium containing solely glucose (Fig 3D and E). Additionally, rates of glycolytic ATP production between groups were only marginally altered despite accounting for the cytoplasmic ATP production linked to mitochondrial glucose oxidation (Fig 3D). We therefore chose not to account for this component, favoring – on balance – an approach where cells are offered complete DMEM to measure rates of oxidative phosphorylation and uncoupled respiration that are not restricted by substrate limitation.

Lastly, prior to applying the method to various models of cell activation, we measured how altered rates of organic acid efflux in response to activation stimuli may affect the measurements. We chose adrenergic activation of brown adipocytes as a model system, as adipocyte lipolysis is known to cause release of fatty acids into the experimental medium (Thompson *et al*, 2010). Fig EV4A–C show that stimulation of brown adipocytes with norepinephrine results in the hallmark increase in uncoupled respiration, as well as an increased rate of H^+ production. To determine whether the contribution of organic acid efflux was different upon norepinephrine stimulation, lactate efflux was measured enzymatically from

matched samples on the same Seahorse XF plate. As before, comparing lactate efflux calculated from the XF Analyzer against that measured from an enzymatic assay was within experimental error of multiple biological replicates (Fig EV4D). However, it was clear that non-glycolytic acid production was increased upon norepinephrine stimulation: the XF Analyzer showed almost a two-fold increase in lactate production in response to adrenergic activation, while the enzymatic assay measured only a 1.5-fold increase (Fig EV4E). This suggests that H^+ measurements were somewhat confounded by differential rates of organic acid efflux (distinct from lactate) upon activation.

Application of the method

ATP production rates show patient-derived glioma xenografts acquire an artificial glycolytic phenotype during in vitro *cell culture*

A clear benefit of measuring ATP production rates is the ability to extend beyond commonly used OCR:ECAR ratios to directly quantify changes in the balance between oxidative phosphorylation and glycolysis. To illustrate this, we analyzed tumor cells from patient-derived glioma xenografts either immediately harvested and purified from mice (~3 h. isolation) or matched cells propagated in *in vitro* gliomaspheres (> 1 week culture period). *In vivo* evidence suggests that the enhanced aerobic glycolysis observed in some glioma cell culture models may be driven, in part, by artifacts of cell selection or *in vitro* growth conditions (Marin-Valencia *et al*, 2012). To explore this, we again confirmed that our measurements of lactate using H^+ efflux matched enzymatic measurements for these patient-derived cultures (Fig 4A). We then examined the information that can be gained from ATP production rates as opposed to OCR:ECAR ratios. In five different cell lines, *in vitro* cultured glioma cells showed a significantly reduced OCR:ECAR ratio compared to matched cells assayed immediately after purification from corresponding murine xenografts (*ex vivo*), indicating a relative shift towards glycolysis in *in vitro* cultured cells (Fig 4B).

Quantifying ATP production rates, however, extends this qualitative analysis. Glioma cells analyzed *ex vivo* just after isolation and purification are highly dependent on oxidative phosphorylation (~70% of total ATP). When cultured *in vitro*, however, cells undergo a remarkable shift in metabolism, increasing their energy demand and switching to glycolysis as the dominant ATP-generating pathway (Fig 4C). Importantly, there is only a slight, statistically insignificant trend towards increased oxidative phosphorylation, suggesting a specific reprogramming of glycolysis acquired upon *in vitro* culture and not simply an increased energy demand met by both pathways. The result shows that calculating ATP production from oxidative phosphorylation and glycolysis yields insights absent in qualitative, ratio-based analyses, and further supports an *in vivo* bioenergetic role of mitochondria in glioblastoma (Maher *et al*, 2012; Mashimo *et al*, 2014).

ATP production rates demonstrate oxidative phosphorylation and glycolysis are differentially engaged upon pro-inflammatory macrophage activation

We then applied our calculation to study pro-inflammatory macrophage activation, a form of immune cell activation associated with substantial metabolic alterations. Upon classical, "type I" activation [LPS (± interferon-γ)], murine BMDMs profoundly remodel energy metabolism away from oxidative phosphorylation (van den Bossche *et al*, 2016; Fig 5A). ATP production is shifted to glycolysis and

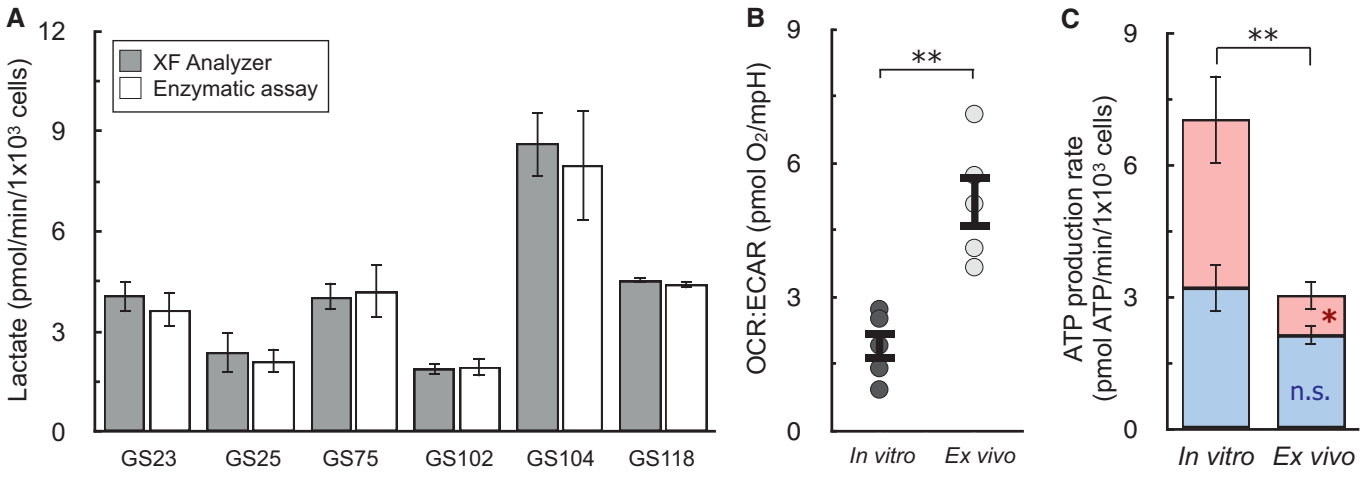

Figure 4. ATP production rates capture changes OCR:ECAR ratios cannot in primary cancer cell models.

A Lactate as measured by the XF Analyzer matches enzymatic lactate measurements for a panel of patient-derived, gliomasphere (GS) cell lines after *in vitro* culture ($n \geq 3$ biological replicates for each line).

B OCR:ECAR ratios for patient-derived glioblastoma cells cultured *in vitro* or assayed immediately after harvesting from mouse xenographs (*ex vivo*). Cell lined used were GS25, GBM39, GS114, GS116, GS122 ($n = 5$ biological replicates).

C ATP Production rates from cell types as in (B) ($n = 5$ biological replicates).

All data are mean ± S.E.M. Statistics were analyzed by a two-tailed Student's *t*-test. *$P < 0.05$; **$P < 0.01$.
Source data are available online for this figure.

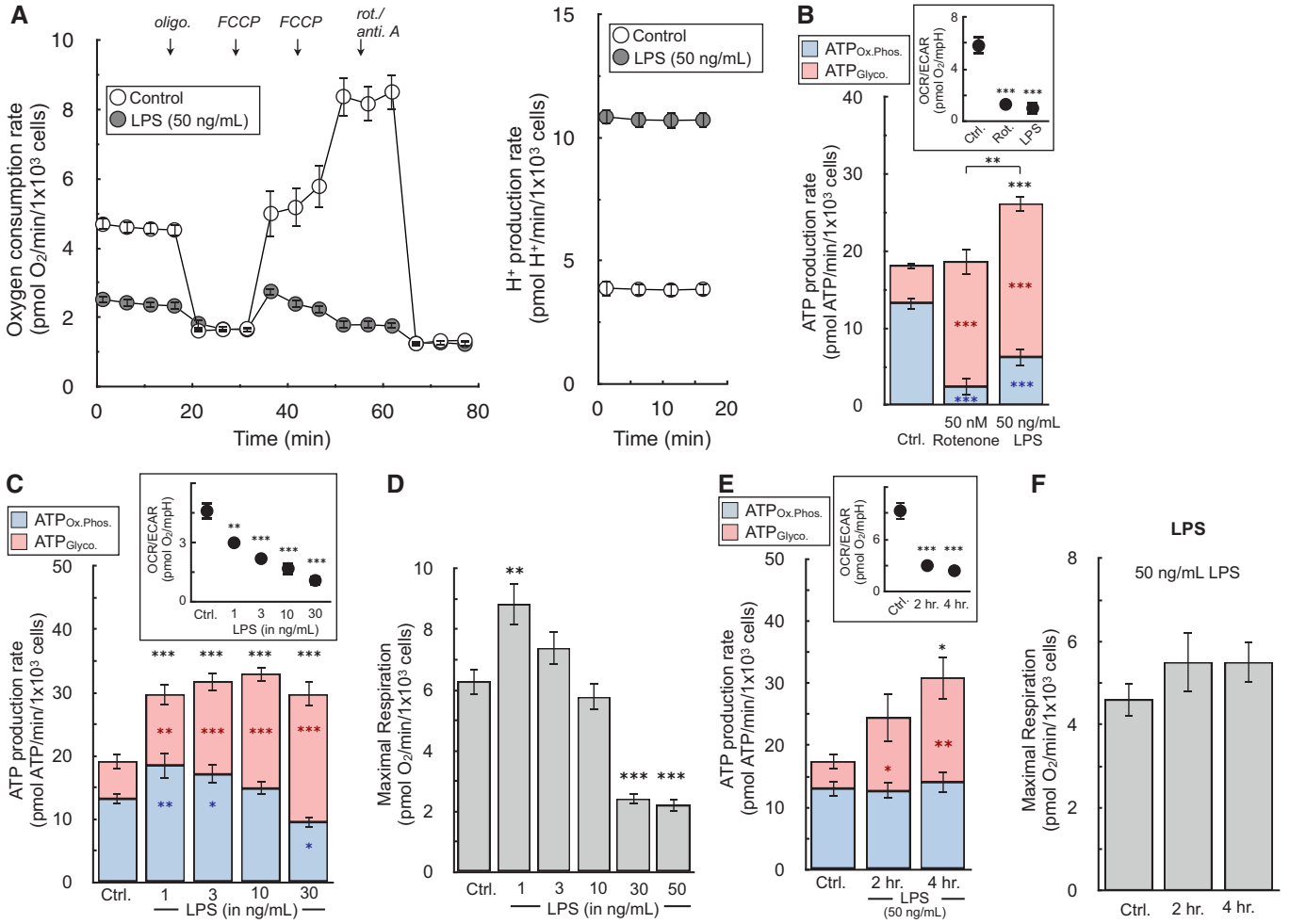

Figure 5. ATP production rates highlight independent regulation of glycolysis and oxidative phosphorylation during LPS activation of macrophages.

A The oxygen consumption rate and H^+ production rate from a representative experiment with BMDMs in response to treatment with 50 ng/ml LPS for 24 h ($n = 5$ technical replicates).

B The ATP production rate is calculated for BMDMs in response to 50 ng/ml LPS or 50 nM rotenone for 24 h. (*Inset*) The OCR:ECAR ratio is presented for each condition ($n = 6$ biological replicates). Representative images used for cell counts are provided in the supplementary material.

C The ATP production rate is calculated for BMDMs in response to varying concentrations of LPS ranging from 1 to 30 ng/ml for 24 h. (*Inset*) The OCR:ECAR ratio is presented for each condition ($n = 5$ biological replicates).

D FCCP-stimulated, maximal respiratory rates from treatments as in (C) ($n = 5$ biological replicates).

E The ATP production rate is calculated for BMDMs in response to treatment for 2 or 4 h. with 50 ng/ml LPS. (*Inset*) The OCR:ECAR ratio is presented for each condition ($n = 4$ biological replicates).

F FCCP-stimulated, maximal respiratory rates from treatments as in (E) ($n = 4$ biological replicates).

All data are mean ± S.E.M. Statistical analysis was analyzed by a one-way, repeated measures ANOVA followed by Dunnett's *post hoc* multiple comparisons tests.
$^*P < 0.05$; $^{**}P < 0.01$; $^{***}P < 0.001$.
Source data are available online for this figure.

mitochondria are repurposed to generate signals that support the pro-inflammatory response (West *et al*, 2011; Lampropoulou *et al*, 2016; Mills *et al*, 2016). By measuring this switch with a qualitative OCR:ECAR ratio, metabolic reprogramming with LPS was indistinguishable from respiratory chain inhibition with complex I inhibitor rotenone (Fig 5B, inset). However, quantifying ATP production rates per cell revealed an increased energy demand associated with LPS activation, discriminating between mitochondrial dysfunction and mitochondrial repurposing during macrophage activation (Figs 5B and EV5).

Quantifying ATP production rates over a range of LPS concentrations further highlights the depth of information gained from the measurements. Qualitative OCR:ECAR ratios in response to increasing LPS concentrations (1–30 ng/ml) suggest a uniform, coordinated shift away from oxidative phosphorylation towards glycolysis to meet ATP demands upon activation (Fig 5C, inset). Cellular ATP production rates, on the other hand, surprisingly reveal these two pathways are engaged independently. Increases in glycolysis and overall ATP utilization are observed with treatments as low as 1 ng/ml LPS, whereas rates of mitochondrial ATP production are not

compromised until LPS concentrations rise above 10 ng/ml (Fig 5C). Additionally, rates of maximal respiration are not compromised at low concentrations of LPS that substantially increase glycolysis, further demonstrating that the increase in glycolytic ATP is not simply a response to impaired mitochondrial oxidative metabolism (Fig 5D).

Indeed, the time-dependence of energetic activation further reveals that regulation of mitochondrial and glycolytic ATP production are disengaged: glycolysis increases within 2 h of activation while rates of oxidative phosphorylation and maximal respiration are maintained up to at least 4 h (Fig 5E and F). The results show the hallmark metabolic changes upon pro-inflammatory macrophage activation are a composite phenotype where increases in ATP demand and glycolysis are controlled distinctly from reductions in oxidative phosphorylation.

ATP production rates can measure healthy bioenergetic changes during cell activation that are lost with static ATP measurements

We finally applied this analysis to models of acute cell activation to highlight the differences between ATP production rates and measurements of ATP content. Healthy cell activation such as neuronal plasma membrane depolarization or T cell receptor activation should minimally affect snapshot-in-time intracellular ATP levels, as cells will readily adapt to a new steady-state of increased ATP turnover (Brand & Nicholls, 2011). In primary cortical neurons, for example, addition of the Na^+-channel activator veratridine stimulates Na^+/K^+-ATPase activity (Fig 6A, top). Both oxygen consumption and extracellular acidification rates increased in response to acute veratridine addition (Choi *et al*, 2009; Fig 6A, bottom). Quantifying ATP production rates showed almost a three-fold increase in the overall rate of ATP turnover upon depolarization, with the balance between oxidative phosphorylation and glycolysis broadly unchanged upon activation (Fig 6B). To demonstrate the sensitivity of the assay, we used a sub-saturating amount of the Na^+/K^+-ATPase inhibitor ouabain (2 nM) to demonstrate the assay can pick up small but meaningful changes in the cellular ATP demand. Large changes in steady-state ATP utilization, however, did not appreciably change static ATP levels, though levels were predictably altered in response to metabolic inhibitors coupled with neuronal depolarization (Fig 6C).

To further demonstrate the principle that ATP production rates provide information during cell activation lost with steady-state measurements, we measured human $CD4^+$ T cell activation in response to anti-CD3/CD28 stimulation. Here again, acute cell activation increased rates of both OCR and ECAR (Fig 6D). As is well documented, T cell activation caused a pronounced increase in glycolysis to meet the energetic and biosynthetic demands of proliferation, cytokine production, and clonal expansion (Maciver *et al*, 2013; Buck *et al*, 2017). Nonetheless, despite a four-fold increase in glycolytic ATP production, comparing both pathways showed oxidative phosphorylation remained the primary source of cellular ATP production, reinforcing an important role for mitochondria during early T cell activation (Sena *et al*, 2013; Fig 6E). As was demonstrated previously for neurons, a physiological increase in the ATP demand that is readily met by T cells did not manifest in substantially altered ATP levels (Fig 6F). In total, the results show real-time ATP production rates can reveal activation-associated changes in energy metabolism that static ATP levels cannot.

Discussion

ATP fluxes during cell activation

Our empirical approach to adjust proton efflux rates for respiratory acidification enables quantification of lactate efflux using OCR and ECAR. Furthermore, obtaining quantitative lactate readouts from the XF Analyzer allows estimation of cellular ATP production rates. ATP production rates from both oxidative phosphorylation and glycolysis provide additional insight into how ATP utilization is distributed during cell adaptation and activation. For example, *in vivo* stable isotope tracing has shown that *in vitro* models of glioblastoma and other cancers can overestimate the contribution of glycolysis to energy metabolism (Marin-Valencia *et al*, 2012; Faubert *et al*, 2017; Momcilovic *et al*, 2019). In support of this, matched samples of patient-derived glioblastoma cells clearly show the acquisition of an artificially high ATP demand driven almost entirely by a five-fold increase in glycolysis in cells cultured *in vitro* relative to those assayed immediately after isolation from murine orthotopic xenografts.

Additionally, the assay reveals that cells can adjust the balance of ATP production differently depending on the type of activation and biological context. As an example, acute activation of the Na^+/K^+-ATPase in primary cortical neurons increases the ATP demand in a way that does not broadly change the proportion of ATP produced by oxidative phosphorylation and glycolysis. Despite an acute, 2.5-fold increase in ATP production, the balance between the two pathways remained roughly constant with about 85% of the total ATP produced by mitochondria. It is sometimes stated that the Na^+/K^+-ATPase and other plasma membrane ATPases preferentially rely on ATP produced by glycolysis (Epstein *et al*, 2014; Sepp *et al*, 2014). However, our results do not support this relationship, at least in two-dimensional cell culture models not subject to microenvironmental gradients.

Unlike the instantaneous increase in ATP demand elicited by plasma membrane depolarization, immune cell activation shows that cells can redistribute the balance between oxidative phosphorylation and glycolysis when activating appropriate signaling cascades. Both T cell antigen receptor (TCR)-linked activation of human T cells as well as TLR-mediated activation of murine macrophages demonstrated that the increase in ATP utilization upon cell activation was increasingly met by glycolysis relative to the naïve state. In T cells this increased glycolytic flux supports generation of biosynthetic intermediates necessary for cell growth and expansion (Maciver *et al*, 2013). Given that many types of TLR activation cause growth arrest in murine macrophages, the observed increase in glycolysis serves a different role. For example, the increase in glycolysis is likely associated with increased flux through the pentose phosphate pathway to support cytoplasmic NADPH production and fuel the anti-microbial NADPH oxidase (Cathcart, 2004). In fact, the approach highlights that regulation of glycolysis and oxidative phosphorylation are disengaged during the pro-inflammatory activation of macrophages. Rather than a coordinated process where mitochondrial ATP production decreases alongside a matched increase in glycolysis, pro-inflammatory stimuli can substantially increase glycolysis without changing rates of oxidative phosphorylation.

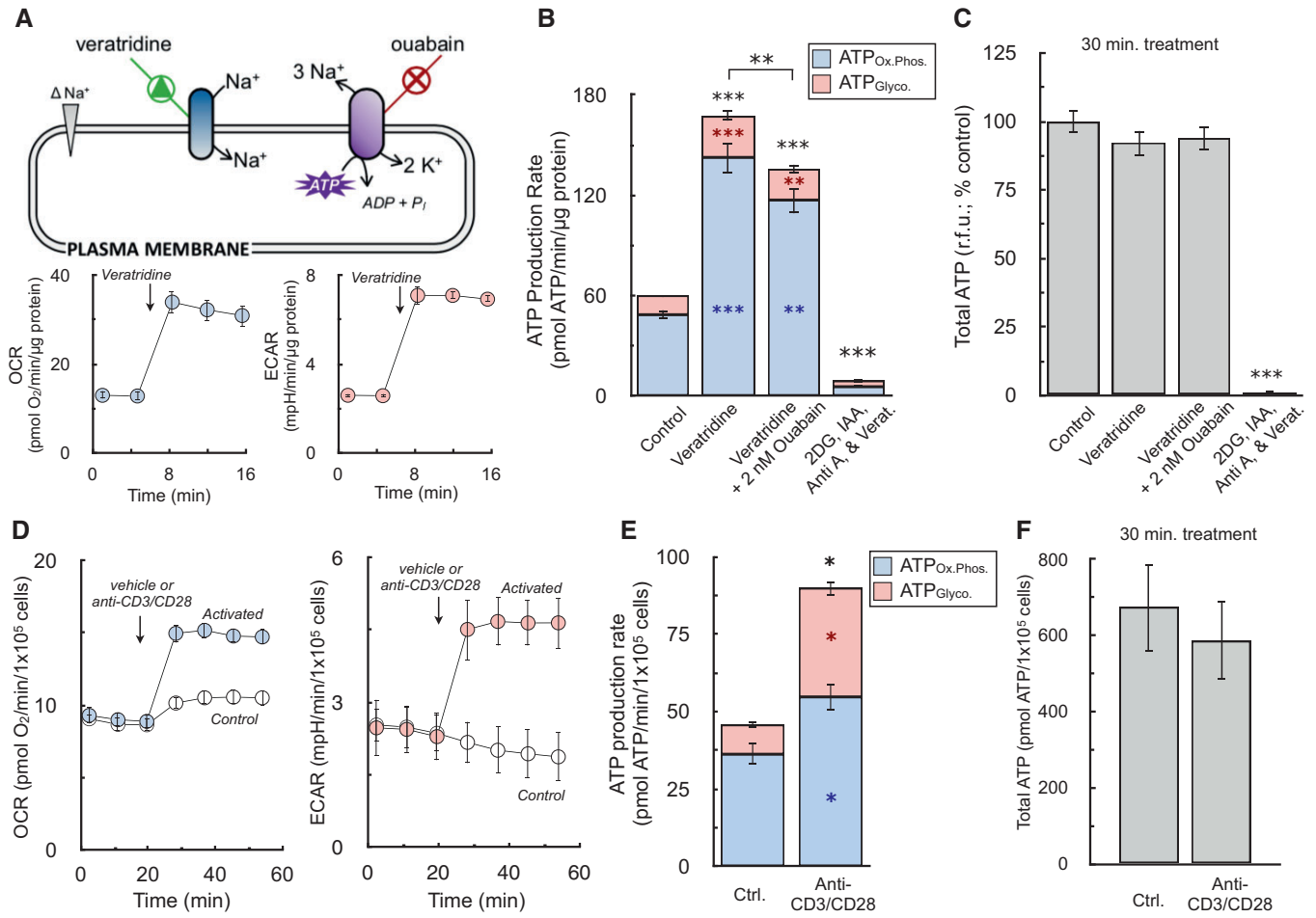

Figure 6. ATP production rates capture healthy changes in cell activation that static ATP measurements cannot.

All data are mean ± S.E.M. unless otherwise specified. *$P < 0.05$; **$P < 0.01$; ***$P < 0.001$.

A (*Top*) Schematic depicting increase in Na^+/K^+-ATPase activity by veratridine, which will depolarize the plasma membrane by increasing sodium influx, thereby triggering ouabain-sensitive increases in ATP production. (*Bottom*) Sample kinetic traces of OCR and ECAR in primary neurons upon acute addition of 1.5 µM veratridine ($n = 10$ technical replicates).

B ATP production rates from oxidative phosphorylation ($ATP_{Ox.Phos.}$, blue) and glycolysis ($ATP_{Glyco.}$, red) in response to (*left to right*) vehicle, 1.5 µM veratridine, veratridine plus 2 nM ouabain to demonstrate sensitivity of the assay, and veratridine plus 1 µM antimycin, 5 mM 2-deoxyglucose, and 1 mM iodoacetic acid to cause an energy crisis and deplete ATP levels ($n = 4$ biological replicates).

C Total ATP levels measured by luminescence after 15 min treatments as in (B) ($n = 4$ biological replicates).

D Sample kinetic traces of OCR and ECAR in murine T cells acutely activated with anti-CD3/CD28 ($n = 4$ technical replicates).

E ATP production rates from oxidative phosphorylation and glycolysis in response to anti-CD3/CD28 ($n = 3$ biological replicates).

F Total ATP levels measured by luminescence after 30 min activation as in (E) ($n = 3$ biological replicates).

All data are mean ± S.E.M. Statistical analysis for 6B and 6C was analyzed by a one-way, repeated measures ANOVA followed by Dunnett's *post hoc* multiple comparisons tests. Individual pairwise comparisons for 6E and 6F were analyzed by a two-tailed Student's *t*-test. *$P < 0.05$; **$P < 0.01$; ***$P < 0.001$.
Source data are available online for this figure.

Adjusting proton production rates to quantify lactate efflux

In line with previous reports (Mookerjee *et al*, 2015), our empirical approach determined that glycolytic and respiratory acidification were the only dominant contributors to the extracellular acidification rate under normal assay conditions. By and large, other reactions that could result in a net pH change of the medium and alter the H^+ efflux rate either (i) did not have with fluxes comparable to those of respiratory and glycolytic acidification, or (ii) occurred proportionally with respiratory CO_2 evolution or lactate efflux (e.g. CO_2 evolution from the pentose phosphate pathway) and fell within a reasonable margin of experimental error. Cell types or experimental conditions that may deviate from this framework are addressed in the "Best practices" section of the Discussion.

Although we demonstrate that the H^+ efflux rate can quantitatively measure lactate efflux after accounting for respiratory CO_2, the empirical values obtained did not follow the expected stoichiometry for either lactate:H^+ or H^+:O_2 and were inconsistent with prior work (Mookerjee *et al*, 2015). These deviations from expected stoichiometry presented here, however, have theoretical and experimental

support. The value of 1.53 ± 0.12 for the lactate:H^+ can be partially explained by incomplete coverage of the plate well by the fluorometric sensor in the XF cartridge, as cells in the center of the well have a far greater effect on the readings than those on the rim.

In fact, the expected lactate:H^+ value of ~1 is obtained when cells are only within a circle connecting the three microplate risers, roughly corresponding to the XF96 fluorometric sensor area. The demonstration that cells directly under the measurement sensor are preferentially, if not exclusively, read by the cartridge suggests that there is no systematic error with the enzymatic lactate measurements. Additionally, the result implies a 1:1 lactate:H^+ ratio should never have been expected, particularly in older instruments where the fluorometric sensors consist of two small spots (Gerencser *et al*, 2009) and not the larger smears found in newer instruments. Seahorse XF Wave software now incorporates this correction into the Proton Efflux Rate (PER) parameter for all multi-well platforms, accounting for the buffering power of the medium and incorporating the geometric corrections obtained from this work.

The H^+:O_2 values from our analysis also deviate from theoretical stoichiometries expected from the complete oxidation of known substrates. Nonetheless, the obtained values change with the appropriate directionality and magnitude in response to oxidizing varying energy substrates in both intact cells and isolated mitochondria. Moreover, lactate efflux rates calculated from the XF Analyzer using an H^+:O_2 of 0.38 ± 0.05 to adjust for respiratory CO_2 matched enzymatic lactate assays, suggesting there was no systemic error in measuring buffering power of the experimental medium.

The discrepancy between the obtained and expected H^+:O_2 values persists in isolated mitochondria, where the experiments are highly controlled and the metabolic reactions are well defined. In this system, the apparent H^+:O_2 values for a truncated reaction where mitochondria are offered pyruvate and malate to generate citrate (theoretical H^+:O_2 = 1 (Mookerjee *et al*, 2015)) are more than 3-fold lower than what is expected in principle and previously observed. The result is likely due, in part, to the different ways the XF Wave software calculates rates of H^+ efflux and O_2 consumption. While the reported rates of H^+ production are a straightforward measurement, the instrument reports rates of O_2 consumption only after an empirical correction to deconvolute the effects of back-diffusion of ambient oxygen into the measurement microchamber (Gerencser *et al*, 2009). This includes use of an 'apparent chamber volume' that is 3-times greater than the actual measurement chamber volume to account for oxygen storage in the walls of the polystyrene microplate, and the algorithmic constants were determined by matching respiration rates obtained from synaptoneurosomes in the XF Analyzer with values obtained from a platinum-based oxygen electrode (Gerencser *et al*, 2009).

Crucially, these corrections would necessarily account, at least partially, for respiration in material along the rim of the plate unseen by the measurement sensor because they are clamped to values obtained from a Clark-type electrode. However, no such corrections for material unseen by the measurement sensor are made for rates of medium acidification. As such, it is expected that rates of H^+ production are consistently underestimated relative to rates of O_2 consumption, and that the observed H^+:O_2 ratios fall below theoretical predictions. Put simply, while software corrections adjust OCR to reflect the full well, this is not the case when measuring H^+ production.

Assumptions and limitations in calculating ATP production rates

Notwithstanding the deviation from expected values, the consensus values obtained for lactate:H^+ and the H^+:O_2 accurately adjust for respiratory CO_2 and can be used to quantitatively reflect lactate efflux. They can therefore be used to convert oxygen consumption rates and H^+ efflux rates into estimates of ATP production as detailed in Datasets EV2–EV4.

Any approach to estimate an ATP production rate, be it the empirical approach presented here or ones based on theoretical principles (Mookerjee *et al*, 2017), are subject to limitations and rely on multiple assumptions. Our empirical approach uses an average H^+:O_2 value for use with standardized experiment medium for cellular bioenergetics: DMEM supplemented with glucose, glutamine, and pyruvate. This approach, however, precludes the ability to estimate ATP supply changes upon shifts in cellular substrate preference (e.g. from fatty acids to glucose) in response to external cues. In principle, this could be done by strictly defining the medium composition and applying different H^+:O_2 values based on assumptions or measurements of what substrates are being oxidized.

Additional limitations associated with our approach are (i) use of an approximate P:O value and (ii) an underestimation of glycolytic ATP as described in the results. Both result from conducting experiments in a composite medium more like cell culture conditions with multiple oxidizable substrates available. It is therefore difficult to know, and perhaps unwise to assume, the fractional contribution of individual substrates to the oxygen consumption rate.

We therefore chose to use an approximate P:O ratio and not to account for glycolytic ATP produced during the complete oxidation of glucose. This approach did not significantly alter measurements of glycolytic ATP in A549 lung adenocarcinoma cells, but the experimental conditions substantially increased rates of oxidative phosphorylation and respiratory capacity. The pre-set calculations of the Seahorse Analytical Software Tools follow this framework: they incorporate average H^+:O_2 and lactate:H^+ values, use an approximate P:O ratio, and ignore the glycolytic ATP contribution from complete glucose oxidation.

Best practices for calculating of ATP production rates

Many of the best practices associated with this particular assay are shared with Seahorse XF assays in general. These include optimizing the plating density for suitable rates, ensuring all measurements are conducted with rates at relatively stable steady-states, using the inner 60 wells of the XF96 microplate to avoid temperature and evaporative effects, and following best practices for normalization (Divakaruni & Jastroch, 2022).

When calculating the buffering power of the experimental medium, it is always best practice to use a non-volatile acid (e.g. H_2SO_4) or two distinct calibrations (e.g. one with HCl and one with H_2SO_4) to minimize instrument and operational error. The buffering power should be checked or recalculated when critical parts of the measurement process are changed – such as switching cartridge lot numbers, batches of medium, or instruments – but does not necessarily need to be calculated alongside each experimental run. In the 96-well instrument, it is often convenient to use

columns 1 and 12 of the microplate for these calculations as is shown in Dataset EV1.

Additionally, it may be that the approximations used for this method are meaningfully inaccurate in specific cases depending on the experimental hypothesis and quantitative rigor required. For example, rates of lactate efflux may be particularly low when using acutely isolated primary cells, and therefore the non-zero background rate of H^+ efflux (Figs 1E and 2C) may represent a substantial component of the signal and skew results. Furthermore, conditions where the rate of lactate efflux is matched by organic acid efflux of the same magnitude may also be less amenable to using consensus values of lactate:H^+ and H^+:O_2. Indeed, this is apparent in noradrenaline-stimulated adipocytes known to release fatty acids: our XF Analyzer calculations based on H^+ release estimated an almost two-fold increase in lactate efflux, whereas the enzymatic assay showed a 1.5-fold increase (Fig EV4). Additionally, under extreme, non-physiological conditions such as neurons depolarized in the absence of glucose, release of glutamate and other neurotransmitters resulted in a profound increase in acidification entirely independent of lactate efflux.

As such, any system in which the investigator believes that non-lactate acid efflux could prohibitively alter the conclusions should consider independently calculating lactate efflux with other methods such as enzymology or mass spectrometry. However, the empirical approach presented here provides the framework for researchers to calculate lactate:H^+ and H^+:O_2 values tailored to any (monolayer) model system or experimental condition.

Materials and Methods

Reagents and Tools table

Reagent/resource	Reference or source	Identifier or catalog number
Chemicals, enzymes, and other reagents		
Oligomycin	Sigma-Aldrich	Cat# 75351
Rotenone	Sigma-Aldrich	Cat# R8875
Antimycin A	Sigma-Aldrich	Cat# A8674
FCCP	Sigma-Aldrich	Cat# C2920
Glucose	Sigma-Aldrich	Cat# G8769
Sodium Pyruvate	Sigma-Aldrich	Cat# P5280
L-Glutamine	Sigma-Aldrich	Cat# G3126
HEPES	Sigma-Aldrich	Cat# 83264
DMEM Powder	Sigma-Aldrich	Cat# 5030
Sodium Chloride	Sigma-Aldrich	Cat# S7653
Phenol Red	Sigma-Aldrich	Cat# P0290
HCl	Sigma-Aldrich	Cat# 2104
H_2SO_4	Sigma-Aldrich	Cat# 1.60315
Water suitable for cell culture	Sigma-Aldrich	Cat# W3500
Software		
Agilent Seahorse XF Wave	Agilent	https://www.agilent.com/en/product/cell-analysis/real-time-cell-metabolic-analysis/xf-software/seahorse-wave-pro-software-2007523
GraphPad Prism	GraphPad	https://www.graphpad.com/
Excel	Microsoft	https://www.microsoft.com/en-us/microsoft-365/excel
Other		
Seahorse XFe96 Analyzer	Agilent	https://www.agilent.com/en/product/cell-analysis/real-time-cell-metabolic-analysis/xf-analyzers/seahorse-xfe96-analyzer-740879
Seahorse XFe96 FluxPak	Agilent	102416-100

Methods and Protocols

Animals and primary cells

All animal procedures were performed in accordance with the NIH Guide for the Care and Use of Laboratory Animals, and approved by the UCLA Animal Research Committee (ARC-2020-027).

Murine bone marrow-derived macrophages (BMDMs)

BMDMs were cultured as previously described (Hsieh *et al*, 2020). Briefly, macrophages were isolated from femurs of male C57BL/6J mice (Jackson 000664) and maintained at 37°C in a humidified 5% CO_2 incubator. Cells were treated with 3 ml RBC lysis buffer (Sigma-Aldrich) to remove red blood cells for 5 min, centrifuged at 386 *g* for 5 min, and resuspended in BMDM culture medium. Culture medium consisted of high-glucose DMEM (Gibco 11965) supplemented with 10% heat-inactivated fetal bovine serum (FBS), 2 mM L-glutamine, 100 U/ml penicillin, 100 μg/ml streptomycin, 500 μM sodium pyruvate, and 5% (v/v) conditioned medium containing macrophage colony stimulating factor (M-CSF) produced by CMG cells to induce differentiation to BMDMs. BMDMs were allowed to differentiate for 6 days, changing medium after 4 days, and then plated for experiments.

Rat cortical neurons

Cortical neurons were generated from embryonic day 18 Sprague–Dawley rats as described previously (Kushnareva *et al*, 2005) and maintained at 37°C in a humidified 5% CO_2 incubator. Cells were plated onto poly-d-lysine-coated wells of black-walled 96-well plates for enzymatic assays or Seahorse XF96 plates. Cells for 96-well plate-based assays were seeded at 2.5×10^4 cells/well and maintained in maintenance medium composed of 200 μl Neurobasal (Thermo Fisher Scientific) medium supplemented with 1× B27 serum-free supplement (Thermo Fisher Scientific), 2 mM GlutaMAX (Thermo Fisher Scientific), 100 U/ml penicillin, and 100 μg/ml streptomycin. Half the medium was replaced every 3–4 days. Experiments in 96-well plates were conducted at day *in vitro* (DIV) 13–17.

Human T cells

Frozen stocks of human naïve $CD4^+$ T cells were purchased from Lonza. Cells were thawed and permitted to recover in RPMI 1640 (Gibco, #11875-085) supplemented with 10% (v/v) FBS at 37°C, 5% CO_2 for 18–24 h. After recovery, cells were spun at 250 *g* for 10 min and resuspended to a final density of 4×10^6 cells/ml in Agilent Seahorse XF RPMI Medium pH 7.4 (#103576-100) supplemented with 10 mM glucose, 2 mM glutamine and 1 mM pyruvate (XF Assay Media). Fifty microliters of the naïve T-cell suspension (2×10^5 cells) were plated in each well of a poly-D-lysine-coated Seahorse XF96 microplate. Plates were spun at 200 *g* for 1 min to adhere cells to the plate. One hundred and thirty microliters of warmed XF Assay Media was then added to each well, and plates were either run in the XF Analyzer or used to measure intracellular ATP concentration with the Cell-Titer Glo Assay (Promega). ATP measurements were taken before and after activation with magnetic Dynabeads coated with anti-CD3/CD28 antibodies (Thermofisher, 4:1 beads/cell).

Additional primary cells preparations

Neonatal rat ventricular myocytes (Rubio *et al*, 2009) and rat cortical astrocytes (Kim & Magrané, 2011) were isolated as previously described. Murine splenocytes were isolated from dissected spleens from C57BL/6 mice. Tissue was mechanically dissociated in HBSS and passed through a 40 μm strainer. Cells were washed and resuspended in red blood cells lysis buffer (Stemcell # 07850) and incubated on ice for 10 min. Cell were washed again in HBSS, passed through a 70 μm filter, counted, and used immediately. For Seahorse XF experiments cells were resuspended in XF Assay Media and seeded at 1.5×10^5 cells/well.

Mitochondrial isolation

Hearts from C57BL/6 mice were drained of blood and homogenized with a hand-held Polytron followed by a Potter-Elvehjem Teflon-on-glass tissue grinder in ice-cold MSHE buffer [70 mM sucrose, 210 mM mannitol, 5 mM HEPES, 1 mM EGTA, and 0.5% (w/v) fatty acid-free BSA] (Kubli *et al*, 2013). The homogenate was centrifuged at 500 *g* for 10 min at 4°C. The supernatant was then collected and centrifuged at 12,000 *g* for 10 min at 4°C to obtain a mitochondrial pellet. The pellet was washed in MSHE and centrifuged at 12,000 *g* for 10 min at 4°C, and this wash step was repeated. Finally, the pellet was resuspended in a small volume (~20 μl) of MSHE, and the protein concentration was determined by Bradford assay.

Cultured cells

All cell lines were obtained from American Type Culture Collection (ATCC) and cultured as suggested by the supplier except when otherwise notified. Each formulation of medium was supplemented with 10% (v/v) fetal bovine serum (FBS), 2 mM GlutaMAX, 100 U/ml penicillin, and 100 μg/ml streptomycin unless otherwise specified. All cells were maintained at 37°C in a humidified 5% CO_2 incubator. Cell lines were maintained in the medium listed parenthetically: A549 [DMEM/F12 (Gibco 11330)]; HepG2 [MEM (Gibco 11095)]; HCT116 [RPMI (Gibco 11875)], C2C12 [DMEM (Gibco 11960 + 2 mM glutamine + 1 mM pyruvate)], A431 [DMEM (Gibco 11960) + 2 mM glutamine + 1 mM pyruvate], BAEC [DMEM (Gibco 11054)], BT474 [ATCC Hybri-Care Cat#46-x], H460 [RPMI (Gibco 11870), 1 mM HEPES, 4 mM glutamine, 5% FBS], HUVEC [EGM Endothelial Cell Growth Medium (Lonza CC-3124)], Jurkat [RPMI (Gibco A10491-01)], MCF7 [RPMI (Gibco 21870 + 2 mM glutamine + 1 mM pyruvate)], MCF-10A [MEBM supplemented with Kit CC-3150 (Lonza) and 100 ng/ml cholera toxin (Sigma)], MDA-MB231 [RPMI (Gibco 21870 + 2 mM glutamine + 1 mM pyruvate)], PC12 [RPMI (ATCC 30-2001+ 2 mM glutamine + 10% Horse Serum + 5% FBS)], Raw 264.7 [DMEM (Gibco 11960) + 2 mM glutamine + 1 mM pyruvate].

3T3-L1 pre-adipocytes and differentiation

3T3-L1 pre-adipocytes were maintained below ~70% confluency in DMEM (Gibco 11965) supplemented with 10% (v/v) bovine calf serum (BCS), 100 U/ml penicillin, and 100 μg/ml streptomycin. For differentiation, cells were plated on Day 2 and were allowed to reach confluency over 48 h. Differentiation was induced on Day 0 by addition of fresh medium with FBS replacing BCS and supplemented with the following: 0.5 mM IBMX, 0.25 μM dexamethasone, 1 μg/ml insulin, and 100 nM rosiglitazone. On Day 2, medium was replaced to DMEM + FBS supplemented with only 1 μg/ml insulin, and thereafter insulin was removed when replacing medium every 2 days.

Immortalized brown adipocytes

Immortalized human brown adipocytes were maintained as described previously (Panic *et al*, 2020). Briefly, cells were cultured in DMEM supplemented with 25 mM glucose, 10% (v/v) fetal bovine serum, 4 mM glutamine, 1 mM sodium pyruvate, 10 mM HEPES, and 100 U/ml penicillin with 100 μg/ml streptomycin. Cells were plated at 1×10^4 cells/well and reached total confluency after approximately 24 h. Medium was then changed to induction medium consisting of the growth medium as before supplemented with 1 μM rosiglitazone, 0.5 mM IBMX, 0.5 μM dexamethasone, 125 μM Indomethacin, 1 nM T3, and 4 nM human insulin. After 2 days, medium was changed to growth medium supplemented with only rosiglitazone and insulin (concentrations as before), and this medium composition was used to change the fluid every other day for an additional 5–6 days.

Seahorse XF analysis

All oxygen consumption and extracellular acidification measurements were conducted using an Agilent Seahorse XF96 or XF^{e}96 Analyzer. Experiments were conducted at 37°C and at pH 7.4 (intact cells) or 7.2 (isolated mitochondria). For experiments with cultured cells, only the inner 60 wells were used, and the outer rim was filled with 200 μl of PBS throughout the incubation to minimize variance in temperature and evaporative effects across the plate (Lundholt *et al*, 2003). All respiratory parameters were corrected for non-mitochondrial respiration and background signal from the instrument with addition of 200 nM rotenone and 1 μM antimycin A. Where appropriate, oligomycin was used at 2 μM unless otherwise specified, and FCCP concentrations were titrated to determine an optimal concentration for a given experiment. Unbuffered DMEM assay medium is composed of DMEM (Sigma #5030; pH 7.4) supplemented with 31.6 mM NaCl, 3 mg/l phenol red, and 5 mM HEPES unless otherwise indicated.

XF analysis primary cortical neurons

All experiments with primary cortical neurons were conducted in a custom, modified Neurobasal-type medium (Divakaruni *et al*, 2017) rather than DMEM to maintain appropriate osmolarity. Glutamine was omitted from the assay medium to minimize excitotoxic injury.

Acid injections and calculation of buffering power

Sequential injections of 62.5 nmol H^+ (25 μl of 1.25 mM H_2SO_4) were made using the Seahorse XF injector ports into unbuffered DMEM assay medium (see above) supplemented with 8 mM glucose, 2 mM glutamine, 2 mM pyruvate and HEPES as indicated in the text. Values were corroborated with matched experiments using 2.5 mM HCl made from freshly purchased stocks no more than 2 months old. Calculations were made using a measurement microchamber volume of 2.28 μl. Step-by-step sample calculations for using the buffering power of the medium to convert ECAR (mpH/min) to pmol H^+/min are provided in Dataset EV1.

Calculation of lactate:H^+ and H^+:O_2

Rates of medium acidification without contribution from respiration were calculated as follows: DMEM assay medium was supplemented with 5 mM glucose and varying concentrations of 2-deoxyglucose (2-DG) and 5 mM iodoacetate (IA) where indicated in the figure. Medium was also supplemented with 200 nM rotenone (to block complex I), 1 μM antimycin A (to block complex III), and 2 μM oligomycin (to block ATP hydrolysis and prevent an energy crisis). Rates were calculated for 75 min, and the spent medium was immediately harvested from each plate and frozen at −80°C for later calculation of endpoint lactate concentration by enzymatic assay (Mookerjee *et al*, 2015). Endpoint lactate values were used to calculate lactate efflux rates.

Rates of medium acidification in the absence of glycolysis were calculated as follows: DMEM assay medium was supplemented with 5 mM pyruvate and 5 mM glutamine (no glucose was provided) along with 2 mM 2-DG and 50 μM IA (to block residual glycolysis and glycogenolysis). 500 U/ml carbonic anhydrase was added to ensure rapid CO_2 hydration, though it was later determined to have a negligible effect on rates of acidification. Respiratory rates were titrated by addition of oligomycin, FCCP (500 nM or 1 μM), and rotenone with antimycin A. The medium was also supplemented with varying concentrations of both UK5099 and BPTES (3 nM to 3 μM for both) to further titrate the respiratory rate. Experiments with primary cortical neurons were conducted in custom medium lacking glutamine as described earlier.

Patient-derived glioblastoma cultures

Patient-derived high-grade gliomas were isolated, purified, and maintained as cell lines or implanted as orthotopic xenografts according to previously published protocols (Gosa *et al*, 2019). Cultured cells (*in vitro*) and tumor cells acutely purified from xenografts (*ex vivo*) were seeded onto Cell-Tak-coated XF96 plates (25 μg/well; Corning). Cells were plated at either 4.0×10^4 or 1.0×10^5 based on cell size and the initial oxygen consumption rate, and spun at 600 *g* for 5 min to adhere cells to the well.

Cell activation assays

Cortical neurons were plated at 2.5×10^4 cells/well and acutely activated with 1.5 μM veratridine added via the injector port of the instrument (Choi *et al*, 2009). Where indicated, cells were pretreated with 2 nM ouabain immediately prior to the assay. When activating the NMDA receptor, 100 μM NMDA was acutely given via the injector port to neurons with or without 15 min. pre-treatment of 10 μM MK-801. For these experiments, the custom assay medium was supplemented with 2 mM β-hydroxybutyrate as substrate, as pyruvate could not be used due to complications with measuring glutamate in the medium by a linked enzymatic assay to confirm depolarization and glutamate efflux. For acute, T cell activation, murine anti-CD3/CD28 Dynabeads (Gibco) were added via the injector port as previously described (Gubser *et al*, 2013).

LPS-mediated activation of BMDMs

BMDMs were plated at 5.0×10^4 cells/well for 48 h. prior to cytokine treatment, which lasted for 24 h. unless otherwise specified. Lipopolysaccharide (LPS) was purchased from PeproTech, Inc. (New Jersey, USA) and offered to cells at 50 ng/ml unless otherwise specified in the manuscript.

H^+:O_2 in isolated heart mitochondria

Isolated rat heart mitochondria from male Sprague–Dawley rats between 3 and 4 months old were plated in XF96 plates (1.5 μg/well) or XF24 (4 μg/well) and spun 2,000 *g* for 20 min to adhere mitochondria to the well. Assays were conducted in MAS medium [220 mM mannitol, 70 mM sucrose, 10 mM KH_2PO_4, 5 mM $MgCl_2$,

1 mM EGTA, and 2 mM HEPES (pH 7.2)] supplemented with 0.2% (w/v) fatty acid-free BSA. For all conditions, uncoupler-stimulated respiration was measured in the presence of 2 μM oligomycin and 4 μM FCCP to eliminate effects of ATP synthesis or hydrolysis on the acidification rate. Rates of respiration and acidification were measured under three conditions: (i) pyruvate/malate (P/M): 10 mM pyruvate with 1 mM malate and 2 mM dichloroacetate; (ii) pyruvate/malate with an inhibitor mix to block various enzymes to run a truncated TCA cycle (P/M/truncated): 10 mM pyruvate with 1 mM malate, 2 mM dichloroacetate, 60 μM fluorocitrate (to block isocitrate dehydrogenase), 2 mM malonate (to block succinate dehydrogenase), and 1 mM aminooxyacetate (to block transaminase activity), and (iii) succinate/rotenone (S/R): 10 mM succinate with 2 μM rotenone to consume oxygen without release of CO_2 to acidify the experimental medium (Mookerjee *et al*, 2015).

Normalization of seahorse XF assays to total protein or cell number

Where indicated on the axis, Seahorse XF assays were normalized either to total protein or cell number determined by *post hoc* high-content imaging. When measuring total protein, cells were lysed in RIPA buffer [50 mM Tris, pH 7.4, 150 mM NaCl, 1% (w/v) NP-40, 0.5% (w/v) sodium deoxycholate, and 0.1% (w/v) sodium dodecyl sulfate], boiled, and assayed using the bicinchoninic assay method (ThermoFisher).

When conducting *post hoc* cell counts, Seahorse XF plates were collected after assays, washed with PBS, and fixed overnight with 2% (w/v) paraformaldehyde in PBS. Cells were left fixed up to 2 weeks. On the day prior to counting, 10 ng/ml Hoescht 33342 (ThermoFisher) was added and incubated overnight at 4°C. Cells were counted using a PerkinElmer Operetta high-content, wide-field, fluorescence imaging system (ex./em. 361/497 nm) coupled to Columbus software (Operetta; PerkinElmer, Waltham, MA, USA).

Enzymatic lactate measurements

Enzymatic lactate measurements were determined in the spent medium recovered after an Agilent Seahorse XF assay. Medium was brought to room temperature if previously frozen, and mixed 1:1 with a 2× assay solution of 40 U/ml lactate dehydrogenase (Sigma-Aldrich L3916), 1 M Tris (pH 9.8), 20 mM EDTA, 40 mM hydrazine (Sigma-Aldrich 309400), and 4 mM NAD^+. The reaction velocity was given by NADH fluorescence (ex./em. 340/460) and measured using a Tecan Spark multimode plate reader (Mookerjee *et al*, 2015). Measurements were taken after 2–4 min (readings were taken every 30 s. to determine when stable values were achieved), and calibrated against known lactate concentrations (Sigma-Aldrich L7022). Importantly, lactate standards were made in assay medium matching the experimental medium to account for any effects from millimolar concentrations of pyruvate in some experimental medium. Standard curves were calculated between 0.2 and 100.0 nmol lactate and modeled with a Michaelis–Menten curve using GraphPad Prism 5.0.

ATP content

Cellular ATP content was measured in lysed cells with the Cell Titer Glo assay (Promega) in 96-well plates according to the manufacturer's specifications.

Quantification and statistical analysis

All statistical parameters, including the number of replicates (n), can be found in the figure legends. Statistical analyses were performed using Graph Pad Prism 5 software for Mac OS X. Data are presented as the mean ± SEM unless otherwise specified. Individual pairwise comparisons were performed using two-tailed Student's t-test. For experiments involving two or more groups, data were analyzed by one-way, repeated measures ANOVA followed by Dunnett's post hoc multiple comparisons tests. Data were assumed to follow a normal distribution (no tests were performed). Values denoted as follows were considered significant: $*P < 0.05$; $**P < 0.01$; $***P < 0.001$.

Step-by-step protocol

The protocol provided here is written alongside the Datasets EV1–EV4 for the calculation of ATP production rates. Established, time-tested protocols are available for conducting standardized respirometry assays with the Seahorse XF Analyzer (Pelletier *et al*, 2014) as well as guidelines for best practices (Divakaruni *et al*, 2014; Divakaruni & Jastroch, 2022). As such, this protocol focuses specifically on the calculation of the buffering power of the experimental medium and subsequent ATP production rates from a Seahorse XF assay. These calculations are amenable to standard protocols for respirometry profiling (i.e. measurements of OCR and ECAR in response to sequential additions of oligomycin, FCCP, and rotenone with antimycin A.). The measurement times at which data points are collected follow standard best practices (Divakaruni *et al*, 2014; Divakaruni & Jastroch, 2022), and examples are provided in the Datasets EV1–EV4. Any deviations from standard Seahorse XF analysis are explicitly noted.

Assay preparation

1 If using adherent cells, plate cells of interest on XF96 microplates at the optimal, previously determined density day(s) prior to the assay according to standard best practices. Only plate cells in the inner 60 wells of the microplate to mitigate deleterious effects from temperature and humidity gradients. Cells grown in suspension are to be acutely spun down onto an adhesive-coated microplate immediately prior to the assay. For all assays, columns 1 and 12 of the microplate must not contain cells, as these wells will be used for acid calibrations and determination of the buffering power of the medium.
2 Prepare assay medium by dissolving DMEM powder into 1 l water and adding 1.85 g NaCl (31.6 mM; to control for osmolarity from lack of bicarbonate), 600 μl phenol red (3 mg/l final), and 5 ml HEPES (5 mM final). Fill to 1 l and adjust pH to 7.4 at 37°C.
3 To this base medium add oxidizable substrates of interest. For the experiments presented here, assay medium is composed of this base supplemented with 8 mM glucose, 2 mM glutamine, and 2 mM pyruvate.
4 Prepare injectate solutions in assay medium for standard respirometry profiling (e.g. oligomycin, FCCP, rotenone, and antimycin A) according to established protocols.
5 Prepare acid solutions to be injected in columns 1 and 12 for the acid calibration. Dilute the acid stock solutions in assay medium. The protocol presented here and detailed in the Dataset EV1 shows 62.5 nmol H^+ injected in each port (25 μl of either 2.5 mM HCl or 1.25 mM H_2SO_4).

6 Load injector ports A–D in columns 2–11 with injectates/effector compounds from Step #4.
7 Load injector ports A-D in columns 1 and 12 with HCl or H_2SO_4 solution from step #5. The calculations presented are for 25 µl loaded in each port with a starting assay volume of 150 µl.
8 Follow manufacturer's instructions and/or best practices for warming the Seahorse XF assay cartridge and preparing assay template. In general, a measurement period of 3 min and 2–3 min of mixing is ideal for this assay to allow for stabilization of the pH readings to assess the buffering power.
9 While the sensor cartridge is calibrating, wash the cells (including background wells) a minimum of three times according to manufacturer's instructions and/or best practices. For columns 1 and 12 used for the acid calibrations, use an aspirator and completely remove the medium, and repeat by filling the well with assay medium and fully aspirating. This is to ensure no remaining growth medium or PBS will affect the buffering power calculations. The example shown here uses a starting assay volume of 150 µl, but the calculations can be adjusted to accommodate any starting volume appropriate for the instrument.
10 Run the Seahorse XF assay according to manufacturer's instructions and/or best practices.
11 Normalize the data according to best practices and available equipment. The data presented here are normalized using nuclear staining (Hoescht) and *post hoc* high-content imaging of the XF microplate (Perkin-Elmer Operetta), but this may not be feasible for all. Guidelines for other, practical means of normalization are discussed in Divakaruni & Jastroch (2022).

Calculation of buffering power (Dataset EV1)

12 Calculate the average value of the last 5 pH recordings prior to the injection of an acid solution (or injectates used in background wells) as shown in rows 3–30.
13 Calculate the change in pH after each injection. Correct for any background drift as shown in cells F32-38
14 Plot the change in pH against the amount of acid added to the microchamber as shown in rows 32–38 or Fig 1B of the manuscript. Downstream calculations are easiest when accounting for the 2.28 µl volume of the XF96 microchamber (see N32-38). Please note that values obtained for a slope in ΔpH/nmol H^+ are equivalent to ΔmpH/pmol H^+. The slope of this graph (plotting F32-38 vs. N32-38) will be used to convert ECAR into pmol H^+/min.

Conversion of ECAR to pmol H^+/min (Dataset EV2)

15 Calculate the average rate of the last two ECAR reading prior to the first injection. This averaged ECAR is then divided by the calculated buffering power yielding the proton production rate (see equation in worksheet). Repeat for each technical replicate. Sample calculations of H^+ production rates for macrophages treated with 50 ng/ml of LPS are presented.

Calculation of required OCR parameters (Dataset EV3)

16 Calculate the basal mitochondrial respiration rate, ATP-linked respiration rate, and proton leak-linked respiration rate using the average of the last two measurements prior to injection. Parameters and best practices are defined in (Divakaruni *et al*, 2014; Divakaruni & Jastroch, 2022) are determined for each technical replicate presented here. Sample calculations of OCR parameters for macrophages treated with 50 ng/ml of LPS are presented.

Calculation of ATP production rates (Dataset EV4)

As detailed in the manuscript text, apply the following equations to the OCR and H^+ production rate parameters obtained in EV2 and EV3 to calculate ATP production rates from oxidative phosphorylation (ATP_{OxPhos}) and glycolysis (ATP_{Glyco}). Sample calculations of ATP production rates for macrophages treated for 24 h. with 50 ng/ml of LPS are presented.

- $ATP_{OxPhos} = 5.45*(OCR_{ATP} + 0.1*OCR_{Leak})$
- $ATP_{Glyco} = 1.53*(H^+_{Total} - 0.38*OCR_{Mito})$
- $ATP_{Total} = ATP_{OxPhos} + ATP_{Glyco}$

Data availability

This study includes no data deposited in external repositories.

Expanded View for this article is available online.

Acknowledgements

ASD is supported by National Institutes of Health (NIH) Grants R35GM138003, P30DK063491, and P50CA092131, as well as the W.M. Keck Foundation (995337). BRD is supported by the U.S. Department of Defense National Defense Science and Engineering (NDSEG) Fellowship Program. AEJ was supported by the UCLA Tumor Cell Biology Training Program (T32 CA009056). ABB was supported by the UCLA Chemistry-Biology Interface Training Grant (T32GM136614). SJB is supported by NIH Grants P01HL146358 and R01HL157710. ABB has been granted a license to use BioRender content in this publication (agreement number CV25KDTXV8).

Author contributions

Brandon R Desousa: Data curation; formal analysis; investigation; writing – original draft; writing – review and editing. **Kristen KO Kim:** Data curation; formal analysis; investigation. **Anthony E Jones:** Data curation; formal analysis; investigation; writing – original draft. **Andréa B Ball:** Data curation; formal analysis; investigation; writing – original draft. **Wei Y Hsieh:** Investigation; methodology. **Pamela Swain:** Data curation; formal analysis; investigation; methodology. **Danielle H Morrow:** Methodology. **Alexandra J Brownstein:** Investigation; methodology. **David A Ferrick:** Resources; project administration. **Orian S Shirihai:** Resources; project administration. **Andrew Neilson:** Conceptualization; resources; project administration. **David A Nathanson:** Resources. **George W Rogers:** Methodology. **Brian P Dranka:** Methodology. **Anne N Murphy:** Resources; methodology; project administration. **Charles Affourtit:** Methodology; writing – review and editing. **Steven J Bensinger:** Resources; funding acquisition; methodology. **Linsey Stiles:** Resources; data curation; formal analysis; investigation; methodology; writing – review and editing. **Natalia Romero:** Conceptualization; resources; data curation; formal analysis; supervision; investigation; methodology; writing – original draft; writing – review and editing. **Ajit S Divakaruni:** Conceptualization; resources; data curation; formal analysis; supervision; funding acquisition; investigation; methodology; writing – original draft; project administration; writing – review and editing.

Disclosure and competing interests statement

NR, GWR, PS, and AN are currently employees and shareholders of Agilent Technologies. BPD, and DAF were previously employees and shareholders of Agilent Technologies at the time of this study. ASD has previously served as a paid consultant for Agilent Technologies.

References

Affourtit C, Brand MD (2009) Measuring mitochondrial bioenergetics in INS-1E insulinoma cells. *Methods Enzymol* 457: 405–424

van den Bossche J, Baardman J, Otto NA, van der Velden S, Neele AE, van den Berg SM, Luque-Martin R, Chen HJ, Boshuizen MCS, Ahmed M *et al* (2016) Mitochondrial dysfunction prevents repolarization of inflammatory macrophages. *Cell Rep* 17: 684–696

van den Bossche J, O'Neill LA, Menon D (2017) Macrophage immunometabolism: where are we (going)? *Trends Immunol* 38: 395–406

Brand MD (2005) The efficiency and plasticity of mitochondrial energy transduction. *Biochem Soc Trans* 33: 897–904

Brand MD, Nicholls DG (2011) Assessing mitochondrial dysfunction in cells. *Biochem J* 435: 297–312

Buck MD, Sowell RT, Kaech SM, Pearce EL (2017) Metabolic instruction of immunity. *Cell* 169: 570–586

Cathcart MK (2004) Regulation of superoxide anion production by NADPH oxidase in monocytes/macrophages: contributions to atherosclerosis. *Arterioscler Thromb Vasc Biol* 24: 23–28

Chandel NS (2015) *Navigating metabolism*. New York, NY: Cold Spring Harbor Laboratory Press

Chen CT, Shih YRV, Kuo TK, Lee OK, Wei YH (2008) Coordinated changes of mitochondrial biogenesis and antioxidant enzymes during osteogenic differentiation of human mesenchymal stem cells. *Stem Cells* 26: 960–968

Choi SW, Gerencser AA, Nicholls DG (2009) Bioenergetic analysis of isolated cerebrocortical nerve terminals on a microgram scale: spare respiratory capacity and stochastic mitochondrial failure. *J Neurochem* 109: 1179–1191

DeBerardinis RJ, Chandel NS (2020) We need to talk about the Warburg effect. *Nat Metab* 2: 127–129

Divakaruni AS, Jastroch M (2022) A practical guide for the analysis, standardization and interpretation of oxygen consumption measurements. *Nat Metab* 4: 978–994

Divakaruni AS, Paradyse A, Ferrick DA, Murphy AN, Jastroch M (2014) Analysis and interpretation of microplate-based oxygen consumption and pH data. *Methods Enzymol* 547: 309–354

Divakaruni AS, Wallace M, Buren C, Martyniuk K, Andreyev AY, Li E, Fields JA, Cordes T, Reynolds IJ, Bloodgood BL *et al* (2017) Inhibition of the mitochondrial pyruvate carrier protects from excitotoxic neuronal death. *J Cell Biol* 216: 1091–1105

Ducker GS, Rabinowitz JD (2017) One-carbon metabolism in health and disease. *Cell Metab* 25: 27–42

Epstein T, Xu L, Gillies RJ, Gatenby RA (2014) Separation of metabolic supply and demand: aerobic glycolysis as a normal physiological response to fluctuating energetic demands in the membrane. *Cancer Metab* 2: 7

Faubert B, Li KY, Cai L, Hensley CT, Kim J, Zacharias LG, Yang C, Do QN, Doucette S, Burguete D *et al* (2017) Lactate metabolism in human lung tumors. *Cell* 171: 358–371

Gerencser AA, Neilson A, Choi SW, Edman U, Yadava N, Oh RJ, Ferrick DA, Nicholls DG, Brand MD (2009) Quantitative microplate-based respirometry with correction for oxygen diffusion. *Anal Chem* 81: 6868–6878

Gillies RJ, Robey I, Gatenby RA (2008) Causes and consequences of increased glucose metabolism of cancers. *J Nucl Med* 49: 24S–42S

Gosa L, Ta L, Nathanson DA (2019) Processing of primary patient tumors and subsequent generation of primary cell lines. *Methods Mol Biol* 1897: 425–431

Gu W, Gaeta X, Sahakyan A, Chan AB, Hong CS, Kim R, Braas D, Plath K, Lowry WE, Christofk HR (2016) Glycolytic metabolism plays a functional role in regulating human pluripotent stem cell state. *Cell Stem Cell* 19: 476–490

Gubser PM, Bantug GR, Razik L, Fischer M, Dimeloe S, Hoenger G, Durovic B, Jauch A, Hess C (2013) Rapid effector function of memory CD8$^+$ T cells requires an immediate-early glycolytic switch. *Nat Immunol* 14: 1064–1072

Hazim RA, Paniagua AE, Tang L, Yang K, Kim KKO, Stiles L, Divakaruni AS, Williams DS (2022) Vitamin B3, nicotinamide, enhances mitochondrial metabolism to promote differentiation of the retinal pigment epithelium. *J Biol Chem* 298: 102286

Hong CS, Graham NA, Gu W, Espindola Camacho C, Mah V, Maresh EL, Alavi M, Bagryanova L, Krotee PAL, Gardner BK *et al* (2016) MCT1 modulates cancer cell pyruvate export and growth of tumors that co-express MCT1 and MCT4. *Cell Rep* 14: 1590–1601

Hsieh WY, Williams KJ, Su B, Bensinger SJ (2020) Profiling of mouse macrophage lipidome using direct infusion shotgun mass spectrometry. *STAR Protoc* 2: 100235

Kim HJ, Magrané J (2011) Isolation and culture of neurons and astrocytes from the mouse brain cortex. *Methods Mol Biol* 793: 63–75

Koveal D, Díaz-García CM, Yellen G (2020) Fluorescent biosensors for neuronal metabolism and the challenges of quantitation. *Curr Opin Neurobiol* 63: 111–121

Kubli DA, Zhang X, Lee Y, Hanna RA, Quinsay MN, Nguyen CK, Jimenez R, Petrosyan S, Murphy AN, Gustafsson ÅB (2013) Parkin protein deficiency exacerbates cardiac injury and reduces survival following myocardial infarction. *J Biol Chem* 288: 915–926

Kushnareva YE, Wiley SE, Ward MW, Andreyev AY, Murphy AN (2005) Excitotoxic injury to mitochondria isolated from cultured neurons. *J Biol Chem* 280: 28894–28902

Lampropoulou V, Sergushichev A, Bambouskova M, Nair S, Vincent EE, Loginicheva E, Cervantes-Barragan L, Ma X, Huang SCC, Griss T *et al* (2016) Itaconate links inhibition of succinate dehydrogenase with macrophage metabolic remodeling and regulation of inflammation. *Cell Metab* 24: 158–166

Lewis CA, Parker SJ, Fiske BP, McCloskey D, Gui DY, Green CR, Vokes NI, Feist AM, Vander Heiden MG, Metallo CM (2014) Tracing compartmentalized NADPH metabolism in the cytosol and mitochondria of mammalian cells. *Mol Cell* 55: 253–263

Lundholt BK, Scudder KM, Pagliaro L (2003) A simple technique for reducing edge effect in cell-based assays. *J Biomol Screen* 8: 566–570

Lunt SY, Vander Heiden MG (2011) Aerobic glycolysis: meeting the metabolic requirements of cell proliferation. *Annu Rev Cell Dev Biol* 27: 441–464

Maciver NJ, Michalek RD, Rathmell JC (2013) Metabolic regulation of T lymphocytes. *Annu Rev Immunol* 31: 259–283

Maher EA, Marin-Valencia I, Bachoo RM, Mashimo T, Raisanen J, Hatanpaa KJ, Jindal A, Jeffrey FM, Choi C, Madden C *et al* (2012) Metabolism of [U-13 C] glucose in human brain tumors *in vivo*. *NMR Biomed* 25: 1234–1244

Marin-Valencia I, Yang C, Mashimo T, Cho S, Baek H, Yang XL, Rajagopalan KN, Maddie M, Vemireddy V, Zhao Z *et al* (2012) Analysis of tumor metabolism reveals mitochondrial glucose oxidation in genetically diverse human glioblastomas in the mouse brain *in vivo*. *Cell Metab* 15: 827–837

Mashimo T, Pichumani K, Vemireddy V, Hatanpaa KJ, Singh DK, Sirasanagandla S, Nannepaga S, Piccirillo SG, Kovacs Z, Foong C *et al* (2014) Acetate is a bioenergetic substrate for human glioblastoma and brain metastases. *Cell* 159: 1603–1614

McConnell HM, Owicki JC, Parce JW, Miller DL, Baxter GT, Wada HG, Pitchford S (1992) The cytosensor microphysiometer: biological applications of silicon technology. *Science* 257: 1906–1912

Mills EL, Kelly B, Logan A, Costa ASH, Varma M, Bryant CE, Tourlomousis P, Däbritz JHM, Gottlieb E, Latorre I *et al* (2016) Succinate dehydrogenase supports metabolic repurposing of mitochondria to drive inflammatory macrophages. *Cell* 167: 457–470

Momcilovic M, Jones A, Bailey ST, Waldmann CM, Li R, Lee JT, Abdelhady G, Gomez A, Holloway T, Schmid E *et al* (2019) *In vivo* imaging of mitochondrial membrane potential in non-small-cell lung cancer. *Nature* 575: 380–384

Mookerjee SA, Goncalves RLS, Gerencser AA, Nicholls DG, Brand MD (2015) The contributions of respiration and glycolysis to extracellular acid production. *Biochim Biophys Acta* 1847: 171–181

Mookerjee SA, Gerencser AA, Nicholls DG, Brand MD (2017) Quantifying intracellular rates of glycolytic and oxidative ATP production and consumption using extracellular flux measurements. *J Biol Chem* 292: 7189–7207

Moyes CD, Mathieu-Costello OA, Tsuchiya N, Filburn C, Hansford RG (1997) Mitochondrial biogenesis during cellular differentiation. *Am J Physiol* 272: C1345–C1351

Newell K, Franchi A, Pouyssegur J, Tannock I (1993) Studies with glycolysis-deficient cells suggest that production of lactic acid is not the only cause of tumor acidity. *Proc Natl Acad Sci U S A* 90: 1127–1131

Nicholls DG, Ferguson SJ (2013) *Bioenergetics*, 4th edn. Cambridge, MA: Academic Press

Panic V, Pearson S, Banks J, Tippetts TS, Velasco-Silva JN, Lee S, Simcox J, Geoghegan G, Bensard C, van Ry T *et al* (2020) Mitochondrial pyruvate carrier is required for optimal brown fat thermogenesis. *Elife* 9: 1–27

Pavlova NN, Thompson CB (2016) The emerging hallmarks of cancer metabolism. *Cell Metab* 23: 27–47

Pelletier M, Billingham LK, Ramaswamy M, Siegel RM (2014) Extracellular flux analysis to monitor glycolytic rates and mitochondrial oxygen consumption. *Methods Enzymol* 542: 125–149

Rich PR, Maréchal A (2010) The mitochondrial respiratory chain. *Essays Biochem* 47: 1–23

Rubio M, Avitabile D, Fischer K, Emmanuel G, Gude N, Miyamoto S, Mishra S, Schaefer EM, Brown JH, Sussman MA (2009) Cardioprotective stimuli mediate phosphoinositide 3-kinase and phosphoinositide dependent kinase 1 nuclear accumulation in cardiomyocytes. *J Mol Cell Cardiol* 47: 96–103

Sena LA, Li S, Jairaman A, Prakriya M, Ezponda T, Hildeman DA, Wang CR, Schumacker PT, Licht JD, Perlman H *et al* (2013) Mitochondria are required for antigen-specific T cell activation through reactive oxygen species signaling. *Immunity* 38: 225–236

Sepp M, Sokolova N, Jugai S, Mandel M, Peterson P, Vendelin M (2014) Tight coupling of Na^+/K^+-ATPase with glycolysis demonstrated in permeabilized rat cardiomyocytes. *PloS One* 9: e99413

Shin B, Benavides GA, Geng J, Koralov SB, Hu H, Darley-Usmar VM, Harrington LE (2020) Mitochondrial oxidative phosphorylation regulates the fate decision between pathogenic Th17 and regulatory T cells. *Cell Rep* 30: 1898–1909

Sullivan WJ, Mullen PJ, Schmid EW, Flores A, Momcilovic M, Sharpley MS, Jelinek D, Whiteley AE, Maxwell MB, Wilde BR *et al* (2018) Extracellular matrix remodeling regulates glucose metabolism through TXNIP destabilization. *Cell* 175: 117–132

Tantama M, Yellen G (2014) Imaging changes in the cytosolic ATP-to-ADP ratio. *Methods Enzymol* 547: 355–371

Thompson BR, Lobo S, Bernlohr DA (2010) Fatty acid flux in adipocytes; the in's and out's of fat cell lipid trafficking. *Mol Cell Endocrinol* 318: 24–33

Watt IN, Montgomery MG, Runswick MJ, Leslie AGW, Walker JE (2010) Bioenergetic cost of making an adenosine triphosphate molecule in animal mitochondria. *Proc Natl Acad Sci U S A* 107: 16823–16827

West AP, Brodsky IE, Rahner C, Woo DK, Erdjument-Bromage H, Tempst P, Walsh MC, Choi Y, Shadel GS, Ghosh S (2011) TLR signalling augments macrophage bactericidal activity through mitochondrial ROS. *Nature* 472: 476–480

Wilson-Fritch L, Burkart A, Bell G, Mendelson K, Leszyk J, Nicoloro S, Czech M, Corvera S (2003) Mitochondrial biogenesis and remodeling during adipogenesis and in response to the insulin sensitizer rosiglitazone. *Mol Cell Biol* 23: 1085–1094

Zhao C, Wilson MC, Schuit F, Halestrap AP, Rutter GA (2001) Expression and distribution of lactate/monocarboxylate transporter isoforms in pancreatic islets and the exocrine pancreas. *Diabetes* 50: 361–366